MASTER THESIS

Modelling for Science and Engineering

Computational study of defects in tungsten-crystals by means of density functional theory

Alba Gordó Vilaseca

September 2018

Universitat Autònoma de Barcelona

Computational study of defects in tungsten-crystals by means of density functional theory

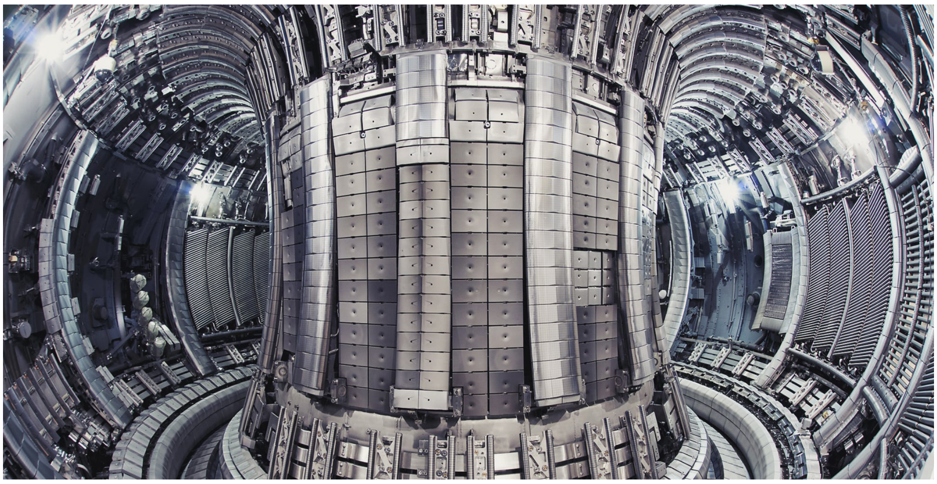

Alba Gordó Vilaseca

Master in Modelling for Science and Engineering
Universitat Autònoma de Barcelona

Under the direction of Dr. Stephan Mohr and Prof. Dr. Mervi J. Mantsinen

Barcelona Supercomputing Centre September 2018

Acknowledgements

En primer lloc, he d'agrair al Dr. Stephan Mohr haver-me brindat l'oportunitat d'endinsar-me en la seva recerca i treballar al seu costat, així com la seva pacient i intensa dedicació en la direcció i supervisió d'aquest treball. M'agradaria donar les gràcies també al Marc Eixarch Fernández, antic alumne de l'Stephan, el treball del qual, [1], ha estat la base d'aquesta tesi.

Agraeixo a la Prof. Dr. Mervi J. Mantsinen la possibilitat que em va donar de pertànyer al Grup de Fusió del Centre de Supercomputació de Barcelona, així com la seva constant atenció i interès pel meu treball. Vull donar les gràcies al Dr. Xavier Sáez i al Dr. Albert Gutiérrez per la seva infinita paciència i la seva ajuda constant, així com al Dani Gallart, pels seus consells i comprensió. També vull tenir un record especial per a la resta de membres del Grup de Fusió, amb els qui he compartit llargues estones de dinar i de qui he après una pila de coses.

Vull agrair a EUROfusion el fet de dotar-nos de les hores de CPU necessàries per realitzar les simulacions dutes a terme al superordinador Marconi, a Itàlia.

També, vull donar les gràcies al Chris, de qui em vull tan a prop, a les dues àvies i a les meves preuadíssimes amigues. Per últim, res d'això no hagués estat possible sense el suport incondicional dels meus pares ni sense la curiositat que m'han estimulat des que era petita; tampoc sense els meus germans, a qui em sento profundament lligada i a qui admiro tant.

Abstract

The characterisation of neutron resistant materials for the plasma facing component armour in a fusion reactor has been established as one of the eight assignments needed to pursue in order to make fusion electricity feasible [2]. So far, tungsten is being regarded as the ‘baseline’ material for this purpose [2]. Understanding the effect of irradiation on materials requires developing atomic-scale models for radiation defects, which describe how the defects evolve and interact [3].

This Master’s thesis tackles the computational study of vacancies in tungsten crystals by means of Density Functional Theory in an implementation of the BigDFT code [4]. As a continuity of the work developed by Marc Eixarch [1], particular emphasis is given to the method used to calculate the energy of systems of different size. This energy is first calculated from scratch for those systems and afterwards using previously generated support functions. The aim of this new approach is to overcome a possible dependence of the "convergence rate" of the support functions with the system size and try to generate a set of consistent results, and it is also faster. A detailed analysis of the correlation between size of the cells, method used and calculated energies has been carried out.

Table of contents

List of figures ix

List of tables xi

1 Introduction 1

1.1 Scientific context . . . 1

1.2 Essentials on fusion research . . . 2

1.3 Tungsten as a material . . . 4

2 Density functional theory and its implementation in BigDFT 5

2.1 The density functional theory (DFT) . . . 5

2.1.1 The Hohenberg-Kohn theorems . . . 7

2.1.2 The Kohn-Sham method . . . 9

2.2 Solid-state physics in a nutshell . . . 11

2.3 Numerical methods and further approximations . . . 13

2.3.1 Pseudopotentials . . . 14

2.3.2 Linear scaling approach . . . 15

2.3.3 Particularities of metallic systems . . . 17

2.4 Wavelets . . . 18

2.4.1 The Haar wavelet family, an iconic approach to wavelets . . . 18

2.4.2 Three dimensional wavelets . . . 21

2.5 BigDFT; the code . . . 21

2.5.1 Implementation of wavelets and resolution levels . . . 22

2.5.2 Implementation of the linear scaling approach . . . 23

3 Study of point defects by means of BigDFT 27

3.1 Brief introduction to point defects . . . 27

3.2 *Ab initio* W-crystal simulations by means of BigDFT . . . 29

3.3 Full system approach 30
3.4 Fragment approach 32
3.4.1 Atomic fragments 35
3.4.2 Onion-alike cluster fragments 36
3.4.3 Two cluster fragments 39
3.5 Brief study of the CPU time consumption 41

4 Conclusions and future work **43**
4.1 Conclusions 43

References **45**

List of figures

1.1 Magnetic confinement devices: tokamak and stellarator 3
1.2 Representations of different atoms distributions; minimal cell and lattice . . 4

2.1 Example of a Wigner-Seitz cell 12
2.2 Representation of the pseudopotential approximation 15
2.3 Density of states in a metal 17
2.4 The Haar scaling function ϕ and the wavelet ψ 19
2.5 Piecewise function by means of the scaling-function of the Haar wavelet . . 19
2.6 Scaling function as linear combination of a scaling function and a wavelet . 19
2.7 Scaling function ϕ and wavelet ψ functions contribution 20
2.8 Least asymmetric Daubechies wavelet family of order $2m = 16$ 22
2.9 Visualisation of the fine and coarse regions of an example molecule 23
2.10 Flowchart of the minimal basis approach 26

3.1 Scheme of two different point defects in a 250-atom tungsten crystal 28
3.2 Formation energies of various perfect and defect configurations 31
3.3 Flowchart of the fragment approach 33
3.4 Visualisation of the fragments 34
3.5 Energy per atom for different perfect crystals through aromic fragmentats . 35
3.6 VFE for different atomic fragmentation for the 250-atoms crystal 36
3.7 VFE for different cluster fragmentations for the 250-atoms crystal 37
3.8 VFE for different cluster fragmentation and system sizes 38
3.9 VFE for different cluster fragmentation and system sizes (bis) 38
3.10 Visualisation of some two cluster shells systems 39
3.11 VFE for different two cluster-shell fragmentations for the 250-atoms crystal 40
3.12 VFE for different 2 cluster fragmentations for the 250-atoms crystal (bis) . 40
3.13 CPU time since initialisation of the template and fragment calculations . . . 41
3.14 CPU time since initialisation of the template and fragment calculations . . . 42

List of tables

2.1 Three-dimensional scaling function and seven three-dimensional wavelets . 21

3.1 Basic parameters used in the full system approach 30
3.2 VFE for different cells in the full system approach 31

Chapter 1

Introduction

1.1 Scientific context

The next decades are crucially important to guiding the world on a path towards lower greenhouse gas emissions. However, the world's population will continue to grow and the proportion of population living in cities is expected to keep increasing [5], which means that even more sustainable energy will be needed later in the century. Nuclear fusion is one of the few zero greenhouse gas emissions energy sources with the potential of replacing fossil fuels. In addition to that, fusion energy is inherently safe, with zero possibility of a meltdown scenario and no long lived waste, and depends on a virtually infinite fuel: water. But so far, this is just a promise and commercial stations are unlikely to materialise before 2050 [6].

Nuclear fusion is the process by which two or more atomic nuclei come close enough to form one or more different atomic nuclei and subatomic particles (neutrons or protons). It is the process that powers stars and trough which the different elements are created. Among all fusion processes, the main reaction fuelling the stars is the combination of light hydrogen atoms (H) to produce the heavier element helium (He) and this is as well the process being regarded to as an energy source on the Earth. In particular, due to its high cross section, the most efficient fusion reaction in the laboratory is the reaction between two hydrogen isotopes; deuterium ${}^{2}_{1}\mathrm{H}$ and tritium ${}^{3}_{1}\mathrm{H}$.

$${}^{2}_{1}\mathrm{H} + {}^{3}_{1}\mathrm{H} \rightarrow {}^{4}_{2}\mathrm{He} + {}^{1}_{0}\mathrm{n} \tag{1.1}$$

The intermediate product of the reaction is an unstable ${}^{5}_{2}\mathrm{He}$ nucleus, which immediately ejects a neutron with $14.1 MeV$. The recoil energy of the remaining ${}^{4}_{2}\mathrm{He}$ nucleus is $3.5 MeV$, so the total energy liberated is $17.6 MeV$ [7].

At very high speeds, when the ionised hydrogen atoms collide, the natural electrostatic repulsion that exists between their positive charges is overcome and the atoms fuse. The mass of the resulting He atom, however, is not the exact sum of the initial H atoms; as Einstein's famous formula $E = mc^2$ describes, some mass m is lost and a great amount of energy E is released [8]. In the Sun core, this process takes place at temperatures of around $1,5 \times 10^7\,K$. However, without the benefit of gravitational forces at work in the Universe and the resulting pressure in the Sun, achieving fusion on Earth has required a different approach and, as explained in Section 1.2, even higher temperatures [6].

Apparently, no known material can cope with that heat, and hence the process needs to be confined in vacuum. Nevertheless, due to the direct contact with its hot edges, the identification and study of suitable materials to construct the container of the nuclear fusion vacuum is of central interest. On top of that, the collision of high-energy neutrons with the wall of the reactor may cause great damage to the material that constitutes it, leading to transmutation of atoms or creation of radiation defects that may evolve to big clusters of defects and eventually change the microstructure of the material. At this point, the material could start to behave unexpectedly or its lifetime be dramatically reduced [9]. Finding a neutron resistant material has been set as one of the eight missions into which the EFDA's 2012 roadmap broke down the quest for fusion energy [2]. Understanding these defects, both qualitatively and quantitatively, is a first step towards this goal and the aim of this work.

Due to the exposure to high heat loads, the research in the field is focused on the study of metallic structures, with high boiling and melting points, what results in fewer impurities in the plasma, as well as high thermal conductivities. Among them, and as will be explained in section 1.3, tungsten (W) is the leading candidate [10–12]. However, considering the infeasibility of experimental studies under such conditions and of studying single point defects at the macroscopic scale, the implementation of computational modelling methods to simulate those situations is requested. In the context of computational materials science, *ab initio* density functional theory methods enable the calculation and prediction of material behaviour on the basis of quantum mechanical considerations, without requiring higher order parameters such as fundamental material properties [13].

1.2 Essentials on fusion research

In order to overcome the electrostatic repulsion between them, the atomic nuclei must have a sufficient speed or temperature. For example, for the deuterium-tritium reaction 1.1, this temperature is $10^9\,K$. However, this temperature is lowered by two reasons: Firstly, having a substance at a certain temperature T, means actually that the average among the temperatures of all its particles is T, meaning that some particles are cooler than T and some hotter. Secondly, due to the quantum tunnelling effect[1], there is a non-zero possibility that nuclei can overcome the electrostatic barrier even with insufficient energy. As a consequence of those two facts, the required temperature lies around $1,5 \times 10^8\,K$. At this temperature, the system is in plasma state, meaning that it is a cloud of electrons, protons and neutrons that lacks a definite shape or volume. Unlike gases, plasmas are electrically conductive, produce magnetic fields and electric currents, and respond strongly to electromagnetic forces.

Since no material can handle such heat, a magnetic field is used to confine plasma in a vacuum. Magnetic fields do not slow down or speed up particles, but are only used to band the trajectories within the plasma. Two main device types fulfilling these characteristics are being investigated for the implementation of nuclear fusion as an energy source; tokamaks and stellarators (see figure 1.1). The difference between a stellarator and a tokamak relies on how the toroidal twisting of the confining magnetic field is generated. Tokamaks do so by driving a plasma current, while stellarators get the magnetic field to bend around by changing the shape of the toroidal coils.

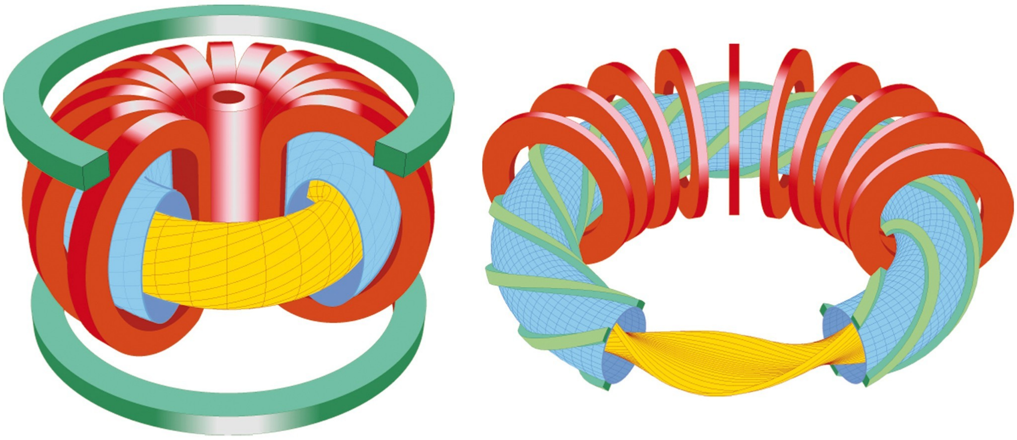

Fig. 1.1 Magnetic confinement devices: tokamak (left) and stellarator (right). In blue, the plasma vessel through which the plasma (yellow) circulates. The toroidal magnetic fields are drawn in red, and green denotes other magnetic field coils (outer poloidal in the tokamak case and helicoidal in the stellarator case). Image from [15].

Even though the magnetic confinement has proven to be extremely efficient, ever escaping highly energetic neutral particles may collide with the bounding walls. Among those particles, the neutrons ejected during reaction 1.1 are the most energetic ones, and hence the ones representing a greater threat. To avoid too frequent replacements, the building element of the reactor walls must be resistant to those events.

---

[1] The quantum tunnelling effect is a a quantum mechanical phenomenon where a particle tunnels through a barrier that it classically cannot surmount [14].

1.3 Tungsten as a material

Tungsten (W) is one of the most promising materials to be used as high-heat-flux material in fusion reactors thanks to its high threshold for sputtering, high melting point and high thermal conductivity [16, 17]. On top of that, W has proven to undergo little erosion under neutron bombardment [10] and plasma–material interaction studies in the ASDEX tokamak indicate W may be a plasma facing material which can provide sufficient lifetime of the first wall components [18, 19]. The use of W on large surface areas in the same tokamak resulted in low plasma impurities and very little W erosion from highly energetic neutral atoms escaping from the plasma [20]. Even though the research on neutron resistant materials considers more and more the use of different alloys to reduce the limitations of the material while accentuating its advantages, the scope of this work focuses only on pure W-crystals.

The most stable phase of W is a body-centred cubic structure (bcc), a type of crystal structure characterised by the minimal cell shown in figure 1.2a. By repeating this cell in space with a translation rule one can build the whole system, as seen in figure 1.2b. The translation vectors of the bcc structure have all the same length and are orthogonal to each other.

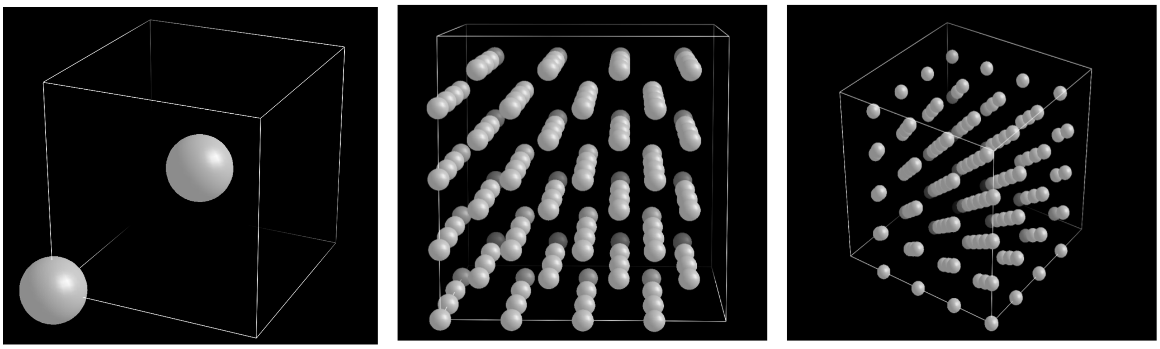

(a) The 2 atoms constituting the minimal cell of a bcc structure.

(b) Perspectives of a 128-atoms bcc lattice.

Fig. 1.2 Representations of different atoms distributions; minimal cell and lattice. Atoms are represented by grey spheres centred at their nuclei’s position. Notice how the lattices in 1.2b are made up of repeating minimal cell blocks of the figure 1.2a type. Images from [1].

Chapter 2

Density functional theory and its implementation in BigDFT

The aim of this chapter is to consider the theoretical background and code-implementation used to tackle the study of the crystallographic system. To do so, we first start by presenting density functional theory and then focus on its implementation in the BigDFT code. Density functional theory is a quantum-mechanical modelling method widely used to investigate the electronic structure of many-body systems. During the analysis of BigDFT, particular attention is given to the code-dependent characteristics of DFT, while further information on specific experimental details is to be presented along the next chapter.

2.1 The density functional theory (DFT)

Any problem in the electronic structure of matter is fully described by the time-dependent Schrödinger equation [21]. In most cases, however, the atoms and molecules considered lack time-dependent interactions, so the time-independent Schrödinger equation may be used instead. For an isolated N-electron system in the Born-Oppenheimer [1] non-relativistic approximation, this is given by

$$\hat{H}\left|\Psi\right\rangle = E\left|\Psi\right\rangle , \tag{2.1}$$

---

[1] The Born–Oppenheimer approximation is the assumption that the motion of atomic nuclei and electrons in a molecule can be separated [22], so that: $\Psi_{\text{total}} = \Psi_{\text{electronic}} \otimes \Psi_{\text{nuclear}}$.

where E is the electronic energy of the wave function [2] $|\Psi\rangle = |\Psi(\mathbf{x}_1,...,\mathbf{x}_N)\rangle$, which depends on the spatial and spin coordinates of electron i (i.e., $\mathbf{r}_i$ and s_i respectively) comprised in $\mathbf{x}_i$. $\hat{H}$ is the Hamiltonian operator, which using atomic units[3] is written as:

$$\hat{H} = \sum_{i=1}^{N}\left(-\tfrac{1}{2}\nabla_i^2\right) + \sum_{i=1}^{N} v(\mathbf{r}_i) + \sum_{i<j}^{N}\frac{1}{r_{ij}}, \tag{2.2}$$

Here, r_{ij} is the distance $|\mathbf{r}_i - \mathbf{r}_j|$ between electron i and electron j and

$$v(\mathbf{r}_i) = -\sum_{\alpha}\frac{Z_\alpha}{r_{i\alpha}} \tag{2.3}$$

is the "external" potential acting on electron i, due to nuclei of charges Z_α placed at a distance $r_{i\alpha} = |\mathbf{r}_i - \mathbf{r}_\alpha|$. Equation 2.2 may be written more compactly as

$$\boxed{\hat{H} = \hat{T} + \hat{V}_{ne} + \hat{V}_{ee}}\ , \tag{2.4}$$

with

$$\hat{T} = \sum_{i=1}^{N}\left(-\tfrac{1}{2}\nabla_i^2\right), \qquad \hat{V}_{ne} = \sum_{i=1}^{N} v(\mathbf{r}_i), \qquad \hat{V}_{ee} = \sum_{i<j}^{N}\frac{1}{r_{ij}}, \tag{2.5}$$

corresponding to the kinetic energy, the electron-nucleus attraction energy and the electron-electron repulsion operators respectively.

The density functional theory of electronic structure is a remarkable theory that allows one to replace the complicated N-electron wave function $|\Psi(\mathbf{x}_1,...,\mathbf{x}_N)\rangle$ and its associated Schrödinger equation by the much simpler electronic density $\rho(\mathbf{r})$ and its associated calculation scheme. In 1964, after a first attempt by Thomas and Fermi [23, 24], Hohenberg and Kohn [25] proved in two theorems that such an approach was possible. This will be shown in the following section. From now on, bear in mind that, if Ψ is normalised, the expectation value of an observable A is given by

$$A[\Psi] = \langle\hat{A}\rangle = \langle\Psi|\hat{A}|\Psi\rangle = \int \Psi^*\hat{A}\Psi d\mathbf{x} \tag{2.6}$$

where $\int d\mathbf{x}$ stands for integration over 3 spatial coordinates and spin. The square brackets denote that Ψ determines A; A is said to be a *functional* of Ψ.

---

[2] In quantum physics, the wave function is a mathematical description of the quantum state of an isolated quantum system.

[3] In Hartree atomic units the following four physical constants are unit by definition: the electron mass m_e, the electron charge e, Planck's constant $\hbar$ and Coulomb's constant k_e.

2.1.1 The Hohenberg-Kohn theorems

The first Hohenberg-Kohn theorem legitimises the use of the electron density $\rho(\mathbf{r})$ as the basic variable, instead of $\Psi(\mathbf{x}_1,...,\mathbf{x}_N)$. In an electronic system, the electron density $\rho(\mathbf{r})$ is defined as the number of electrons per unit volume in a given state, so that

$$\int \rho(\mathbf{r})d\mathbf{r} = N. \tag{2.7}$$

Theorem 1. *The external potential $v(\boldsymbol{r})$ is determined, up to a trivial additive constant, by the electron density $\rho(\boldsymbol{r})$.*

Proof. Consider the electron density $\rho_0(\mathbf{r})$ for the non-degenerate ground state of some N-electron system. $\rho_0(\mathbf{r})$ determines N by simple quadrature 2.7. If there were two external potentials v_1 and v_2 differing by more than a constant, each giving the same ρ_0 for its ground state, two Hamiltonians H_1 and H_2 would arise, whose ground state densities were the same although the normalised wave functions Ψ_1^0 and Ψ_2^0 would be different. Taking Ψ_2^0 as a trial function:

$$E_1^0 < \langle\Psi_2^0|\hat{H}_1|\Psi_2^0\rangle = \langle\Psi_2^0|\hat{H}_2|\Psi_2^0\rangle + \langle\Psi_2^0|\hat{H}_1 - \hat{H}_2|\Psi_2^0\rangle = E_2^0 + \int \rho(\mathbf{r})[v_1(\mathbf{r}) - v_2(\mathbf{r})]d\mathbf{r}, \tag{2.8}$$

where E_1^0 and E_2^0 are the ground state energies for $\hat{H}_1$ and $\hat{H}_2$, respectively. Similarly, taking Ψ_1^0 as a trial function for the $\hat{H}_2$ problem:

$$E_2^0 < \langle\Psi_1^0|\hat{H}_2|\Psi_1^0\rangle = \langle\Psi_1^0|\hat{H}_1|\Psi_1^0\rangle + \langle\Psi_1^0|\hat{H}_2 - \hat{H}_1|\Psi_1^0\rangle = E_1^0 - \int \rho(\mathbf{r})[v_1(\mathbf{r}) - v_2(\mathbf{r})]d\mathbf{r}. \tag{2.9}$$

Adding 2.8 and 2.9, results in $E_1^0 + E_2^0 < E_2^0 + E_1^0$; a contradiction. Hence, there cannot be two different $v(\mathbf{r})$ that give the same ρ at the ground state. □

Since $\rho(\mathbf{r})$ determines both N and $v(\mathbf{r})$, it follows that $\rho(\mathbf{r})$ also determines all the other electronic properties of the system, including its ground state, or lowest-energy state, with wave function $|\Psi_0\rangle$.

Writing E_v instead of E to make the dependency on v explicit, the expectation value of equation 2.4 can be written as follows,

$$E_v[\rho] = V_{ne}[\rho] + F[\rho], \tag{2.10}$$

with

$$F[\rho] = T[\rho] + V_{ee}[\rho]. \tag{2.11}$$

Notice that $F[\rho]$ is defined independently of the external potential $v(\mathbf{r})$, so it is a *universal functional* that depends on $\rho(\mathbf{r})$.

The second Hohenberg-Kohn theorem provides the energy variational principle.

Theorem 2. *For a trial density $\tilde{\rho}(\boldsymbol{r})$, such that $\tilde{\rho}(\boldsymbol{r}) \geqslant 0$ and $\int \tilde{\rho}(\boldsymbol{r})d\boldsymbol{r} = N$,*

$$E_0 \leqslant E_v[\tilde{\rho}], \tag{2.12}$$

where $E_v[\tilde{\rho}]$ is the energy value resulting of applying the functional 2.10 to the given system.

Proof. The previous theorem assures that $\tilde{\rho}$ determines its own $\tilde{v}$, $\tilde{H}$ and $\tilde{\Psi}$, which can be taken as trial function. Thus,

$$\langle\tilde{\Psi}|\hat{H}|\tilde{\Psi}\rangle = \int \tilde{\rho}(\mathbf{r})v(\mathbf{r})d\mathbf{r} + F[\tilde{\rho}] = E_v[\tilde{\rho}] \geqslant E_v[\rho] = \langle\Psi|\hat{H}|\Psi\rangle\,. \tag{2.13}$$

□

Assuming differentiability of $E_v[\rho]$, the variational principle 2.12 requires the ground state density to satisfy the stationary principle

$$\delta\left\{E_v[\rho] - \mu\left[\int \rho(\mathbf{r})d\mathbf{r} - N\right]\right\} = 0, \tag{2.14}$$

which gives the the Euler-Lagrange equation

$$\boxed{\mu = \frac{\delta E_v[\rho]}{\delta\rho(\mathbf{r})} = v(\mathbf{r}) + \frac{\delta F[\rho]}{\delta\rho(\mathbf{r})}}\,. \tag{2.15}$$

where the chemical potential μ is the Lagrange multiplier associated to the constraint 2.7.

Although extremely powerful, in practice the Hohenberg-Kohn theorems do not offer a way of computing the ground state density of a system. About a year after the Hohenberg-Kohn theorems were published, Kohn and Sham [26] devised an approach that made DFT feasible. The Kohn-Sham ansatz is that the exact ground state density can be written as the ground state density of a fictitious system of non-interacting particles. This then gives a set of independent particle equations that can be solved numerically.

2.1.2 The Kohn-Sham method

Let us start by presenting the exact formula for the ground-state kinetic energy

$$T = \langle\Psi| - \sum_i \tfrac{1}{2}\nabla_i^2 |\Psi\rangle \tag{2.16}$$

and reminding that the Hohenberg-Kohn theory assures that T is a functional of $\rho(\mathbf{r})$, which can be written as

$$\rho(\mathbf{r}) = N\sum_{s_1}\cdots\sum_{s_N}\int d\mathbf{r}_2\cdots\int d\mathbf{r}_N\,|\Psi(\mathbf{r},s_1,\mathbf{r}_2,s_2,...,\mathbf{r}_N,s_N)|^2\,. \tag{2.17}$$

For any *interacting* system of interest, Ψ in equations 2.16 and 2.17 may have an infinite number of determinants if built from single particle orbitals as Slater determinants. Kohn and Sham's approach proposed approximating the kinetic energy T of an N *interacting* electrons' system with the kinetic energy T_s of a fictitious system of N *non-interacting* electrons that yield $\rho(\mathbf{r})$. Using the Kohn-Sham method, one ends up using only one determinant. To this end, orbitals $\psi_i(\mathbf{r})$ are introduced, and an equivalent description of T_s and $\rho(\mathbf{r})$ are given:

$$T_s[\rho] = \sum_i f_i\,\langle\psi_i| - \tfrac{1}{2}\nabla^2 |\psi_i\rangle \tag{2.18}$$

$$\rho(\mathbf{r}) = \sum_i f_i\,|\psi_i(\mathbf{r})|^2\,. \tag{2.19}$$

In the previous equations f_i is the Fermi function that determines the occupation of the i-th orbital so that $\sum_i f_i = N$ with $0 \leq f_i \leq 1$.

$$f_i = \frac{1}{1+\exp\left[\frac{\varepsilon_i-\mu}{k_BT}\right]}\,. \tag{2.20}$$

Here, ε_i is the energy of the i-th orbital, μ the chemical potential, k_B Boltzman's constant and T the electronic temperature, often assumed to be zero. Notice that at $T = 0$, f_i equals 1 or 0 (depending on the sign of $\varepsilon_i - \mu$). This case corresponds to the ground state density in which only the N lowest Kohn-Sham orbitals are occupied.

In addition to that, the electron-electron $V_{ee}[\rho]$ interaction term is also rewritten as the Coulomb interaction term $J[\rho]$, which only takes into account the classical interaction between electrons.

$$J[\rho] = \frac{1}{2}\int\int\frac{1}{r_{12}}\rho(\mathbf{r}_1)\rho(\mathbf{r}_2)d\mathbf{r}_1 d\mathbf{r}_2 \tag{2.21}$$

To produce the desired separation out of $T_s[\rho]$ as the kinetic energy component and $J[\rho]$ as the electron-electron interaction, 2.11 is redefined as

$$F[\rho] = T_s[\rho] + J[\rho] + E_{xc}[\rho] \tag{2.22}$$

where

$$E_{xc}[\rho] = T[\rho] - T_s[\rho] + V_{ee}[\rho] - J[\rho] \tag{2.23}$$

is called the *exchange-correlation energy*, which contains the difference between T and T_s, presumably fairly small [13], and the non-classical part of $V_{ee}[\rho]$, including the relativistic dependence of mass on the velocity (see [27] for an introductory explanation).

By doing so, the Euler equation 2.15 becomes

$$\mu = v_{\text{eff}}(\mathbf{r}) + \frac{\delta T_s[\rho]}{\delta \rho(\mathbf{r})}, \tag{2.24}$$

where the *Kohn-Sham effective potential* is defined by

$$v_{\text{eff}}(\mathbf{r}) = v(\mathbf{r}) + \frac{\delta J[\rho]}{\delta \rho(\mathbf{r})} + \frac{\delta E_{xc}[\rho]}{\delta \rho(\mathbf{r})} = v(\mathbf{r}) + \int \frac{\rho(\mathbf{r}')}{|\mathbf{r}-\mathbf{r}'|} d\mathbf{r}' + v_{xc}(\mathbf{r}). \tag{2.25}$$

$v_{xc}(\mathbf{r})$ is the so called *exchange-correlation potential.*

Equation 2.24 with the constraint 2.19 corresponds to equation 2.15 if applied to a system of non-interacting electrons moving in the external potential $v_s(\mathbf{r}) = v_{\text{eff}}(\mathbf{r})$. Therefore, for a given $v_{\text{eff}}(\mathbf{r})$, the $\rho(\mathbf{r})$ that satisfies 2.24 is obtained by solving the N one-electron equations

$$\left[-\tfrac{1}{2}\nabla^2 + v_{\text{eff}}(\mathbf{r})\right] \psi_i = \varepsilon_i \psi_i \qquad i = 1, \ldots, N \tag{2.26}$$

where ε_i are the eigenvalues of the Kohn-Sham orbitals ψ_i.

Equations 2.25-2.26 are the celebrated Kohn-Sham equations, through which the kinetic operator is made particle-independent. However, this comes with a price: the quality of the results will depend on the quality of the exchange-correlation functional $E_{xc}[\rho]$, the exact form of which is unknown. Its value can only be determined through approximations.

For completeness, the final energy functional under the Kohn-Sham approach is written as follows:

$$\begin{aligned} E_{KS}[\rho] &= T_s[\rho] + J[\rho] + E_{xc}[\rho] + \int v(\mathbf{r})\rho(\mathbf{r})d\mathbf{r} \\ &= \sum_i^N \langle \psi_i| -\tfrac{1}{2}\nabla^2 |\psi_i\rangle + \frac{1}{2}\int\int \frac{1}{r_{12}}\rho(\mathbf{r}_1)\rho(\mathbf{r}_2)d\mathbf{r}_1 d\mathbf{r}_2 + E_{xc}[\rho] + \int v(\mathbf{r})\rho(\mathbf{r})d\mathbf{r} \end{aligned} \tag{2.27}$$

Before addressing the numerical methods and approximations required to actually implement DFT, a brief introduction to some important concepts of condensed-matter and solid-state physics need to be discussed. This is done along the following section.

2.2 Solid-state physics in a nutshell

The target category of materials to be considered for the wall of the fusion reactor is restricted to pure metals and metallic alloys, specially containing W, in solid state, which are periodic regular arrangements of atoms (i.e., crystals).

A discrete but infinite regular arrangement of points (lattice sites) in a vector space is called a lattice. Lattices which exhibit a discrete translational symmetry are referred to as Bravais lattices. In the $\mathbb{R}^3$ space, this means that translation of the whole lattice by any translation vector $\mathbf{t}$ leave the lattice unchanged. $\mathbf{t}$ is given by

$$\mathbf{t} = m\mathbf{a}_1 + n\mathbf{a}_2 + o\mathbf{a}_3 \qquad m,n,o \in \mathbb{Z}, \tag{2.28}$$

where a_i are known as the primitive vectors that span the lattice and determine the unit cell dimension. Bravais lattices are completely characterised by equations of this type.

A crystal is defined as a lattice the points of which have been filled in with an atom or group of atoms. To enhance understanding of crystal structures, the concept of cell is introduced. A cell is a small element that can build up the whole crystal without overlaps nor gaps by repetitive arrangement (see figure 1.2b). A cell that contains exactly one lattice point, is named primitive cell. A primitive cell of particular interest is the Wigner–Seitz cell around a lattice point (i.e., atom), which is defined as the locus of points in space that are closer to that lattice point than to any of the other lattice points (see figure 2.1).

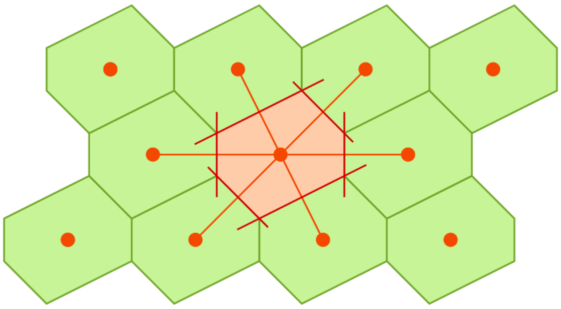

Fig. 2.1 Example of the construction of a Wigner-Seitz cell, where the red dots represent the points or atoms in the Bavais lattice and the green enclosed regions are Wigner-Seitz cells. Image from [28].

A particle in a periodically-repeating environment (e.g., an electron in a crystal) can be described by Bloch waves $\Psi_k(\mathbf{r})$, which are wave functions of the type

$$\Psi_k(\mathbf{r}) = \Psi_0(\mathbf{r}) \cdot e^{i\mathbf{kr}}, \tag{2.29}$$

where $e^{i\mathbf{kr}}$ is a plane wave[4] and $\Psi_0(\mathbf{r})$ is a periodic function with the same periodicity as the crystal. This is the so called Bloch theorem.

The reciprocal lattice is defined as the set of vectors $\mathbf{k}$ for which the corresponding Bloch waves have the periodicity of the Bravais lattice $\mathbf{t}$, so that

$$\Psi_k(\mathbf{r}) \overset{!}{=} \Psi_k(\mathbf{r}+\mathbf{t}) \Leftrightarrow \Psi_0(\mathbf{r}) \cdot e^{i\mathbf{kr}} = \Psi_0(\mathbf{r}+\mathbf{t}) \cdot e^{i\mathbf{k(r+t)}} \Leftrightarrow e^{i\mathbf{kt}} = 1 \Leftrightarrow \mathbf{k}\cdot\mathbf{t} = 2\pi l, \quad l \in \mathbb{Z}. \tag{2.30}$$

This defines a set of vectors $\mathbf{k}$ with respect to the set of Bravais lattice vectors $\mathbf{t}$. The reciprocal lattice is defined similarly to the initial Bravais lattice 2.28

$$\mathbf{k} = p\mathbf{b}_1 + q\mathbf{b}_2 + r\mathbf{b}_3 \qquad p,q,r \in \mathbb{Z}, \tag{2.31}$$

with the restriction $b_i \cdot a_j = 2\pi\delta_{ij}$ arising from equation 2.30. In the same way the Bravais lattice is divided up into Wigner-Seitz cells in the real lattice, the reciprocal lattice is broken up into Brillouin zones (see figure 2.1).

The electronic ground state of a periodic system is usually described in terms of extended Bloch orbitals, simultaneous eigenstates of the periodic Hamiltonian and of the direct lattice translations [29]. Having defined the reciprocal lattice enables an alternative representation in terms of localised orbitals through the so called Wannier functions.

---

[4] A plane wave is a wave whose wave fronts are infinite parallel planes.

In chemistry, localised molecular orbitals are functions that describe the wave-like behaviour of an electron in a molecule concentrated in a limited spatial region. The Wannier functions are a complete set of orthogonal, strictly localised functions that are the analogue to the molecular orbitals for crystalline systems. The simplest and most common definition of Wannier functions is the one based on the Bloch waves 2.29 of a single energy band[5] in a perfect crystal. Then, Wannier functions are defined by

$$\phi_t(r) = \frac{1}{\sqrt{N}} \sum_k e^{-i\mathbf{k}\cdot\mathbf{t}} \Psi_{\mathbf{k}}(\mathbf{r}). \tag{2.32}$$

As localised molecular orbitals, Wannier functions decay exponentially with the distance $\mathbf{r}$ [30].

2.3 Numerical methods and further approximations

The aim of practical calculations is usually to find the final energy given by equation 2.27, for which simple approximations to $E_{xc}[\rho]$ are used. The Kohn-Sham equations 2.25-2.26 are started with an initial guess for the density ρ, yielding a Kohn-Sham potential via equation 2.25. The Kohn-Sham equations are then solved and a new density is found. This cycle is repeated until changes become negligible, *i.e.*, the system is self-consistent [31]. However, the exact functionals for the exchange-correlation potential $v_{xc}(\mathbf{r})$ is only known for the free electron gas. Hence, the basic idea of the approximations is to use the exchange-correlation function $E_{xc}[\rho]$ of an electron gas with the same electron density as the real target system.

∗ *Local (spin) Density approximation* - LDA, which assumes $E_{xc}[\rho]$ depends only on the density at the coordinate where the functional is evaluated

$$E_{xc}[\rho] = \int e_{xc}(\rho(\mathbf{r}))d\mathbf{r}, \tag{2.33}$$

where e_{xc} is the exchange-correlation energy of a uniform gas of density $\rho(\mathbf{r})$. The LDA assumes the density $\rho(\mathbf{r})$ to be the same everywhere. Because of this, LDA has a tendency to underestimate some of the terms in E_{xc} and overestimate some others.

---

[5] In solid-state physics, each of the energies that an electron within the solid may have is called energy band or simply band.

- *Generalised-Gradient approximation* - GGA, which accounts for the non-homogeneity of the true electron density by expanding in terms of the gradient of the density.

$$E_{xc}[\rho] = \int e_{xc}(\rho(\mathbf{r}), \nabla\rho(\mathbf{r}))d\mathbf{r} \tag{2.34}$$

The GGA method results in much better outcomes for more complex systems, at expenses of computational time, and has become the standard.

At this stage, three main issues would still make simulations tough and computationally expensive. Along the following subsections the approaches required to overcome them are tackled.

i. Metals usually have a lot of electrons per atom. Taking into account that each electron implies the calculation of an orbital function, the cost of calculation is proportional to the cube of the electrons-per-atom ratio and may be huge.

ii. The fact that a radiation defect breaks the periodicity of a perfect lattice demands the use of big cells, but DFT simulations scale $O(N^3)$ with the system size.

iii. Metallic systems impose further difficulty in DFT simulations due to their zero energy gap between the highest occupied and lowest unoccupied electronic orbitals (HOMO-LUMO gap).

2.3.1 Pseudopotentials

Electrons close to the core region of an atom are usually not involved in chemical reactions, nor change significantly their atomic features when the atom interacts in a system. In addition to that, the remaining electrons, placed in the valence orbitals, acquire their oscillating behaviour mainly due to orthogonality constraints to the core orbitals (i.e., Pauli's exclusion principle). In the pseudopotential approximation, the original atoms that constitute a given chemical system are modified by removing the core energy levels and replacing the potential of the atomic nucleus and of the core electrons by a *pseudopotential* (see figure 2.2). The Pauli exclusion principle is then enforced through repulsive pseudopotential [32].

It is worth noticing that the use of pseudopotentials does not only decrease the complexity of the calculation by reducing the number of orbitals and avoiding the need of very high resolution around the nuclei, specially in the case of atoms with high atomic number, but also offers the possibility of easily including relativistic effects [33].

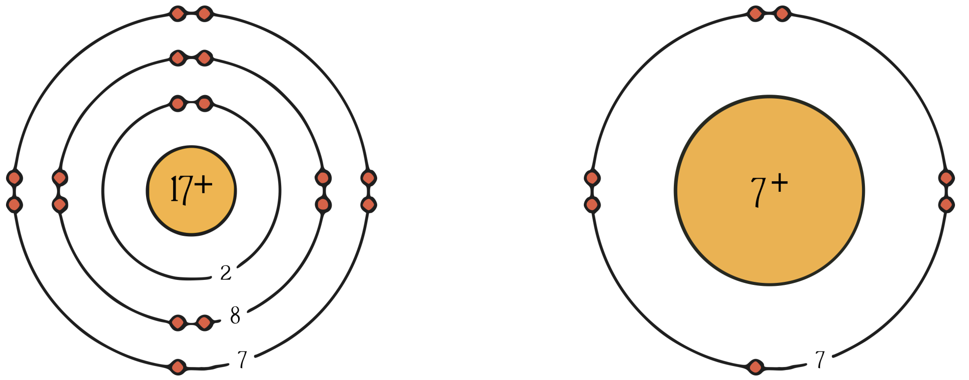

(a) Representation of the atom. **(b)** Representation of its pseudopotential.

Fig. 2.2 Pseudopotential approximation process for a Cl$^-$ atom.

2.3.2 Linear scaling approach

Any approach to the Kohn-Sham equations 2.25-2.26 which involves calculating and manipulating the one-electron functions directly will inevitably scale as $O(N^3)$: at least $O(N)$ orbitals are required, to describe the $O(N)$ electrons occupying them; each orbital extends over the whole system and thus any manipulation of it requires an $O(N)$ effort; and the constraint of mutual orthogonality between these orbitals means that minimisation of the energy can only be achieved with an extra $O(N)$ work [34]. To circumvent this problem, one can exploit Kohn's *nearsightedness principle*, which states that, given a substance at finite temperature (or even at $T = 0$ in the case of non-metals), all its physical quantities are determined by the local chemical environment [35–37].

Within DFT, as seen in section 2.1.2, the total energy can be regarded as a functional of the occupied Kohn-Sham orbitals $\psi_i(\mathbf{r})$ and the ground state can be obtained by minimising the total energy with respect to these orbitals. Equivalently, the total energy can be treated as a functional of the electron density matrix $\rho(\mathbf{r},\mathbf{r}')$ [38], defined as

$$\rho(\mathbf{r},\mathbf{r}') = \sum_i f_i \psi_i(\mathbf{r}) \psi_i^*(\mathbf{r}'). \tag{2.35}$$

where f_i is again the Fermi function 2.20. In this approach, the extended Kohn–Sham orbitals are expressed as a set of localised adaptively contracted basis functions called support functions ϕ_α.

$$\psi_i(\mathbf{r}) = \sum_\alpha c_i^\alpha \phi_\alpha(\mathbf{r}). \tag{2.36}$$

The density matrix 2.35 is then given by

$$\rho(\mathbf{r},\mathbf{r}') = \sum_{\alpha\beta} \phi_\alpha(\mathbf{r}) K^{\alpha\beta} \phi^*_\beta(\mathbf{r}'), \tag{2.37}$$

where $K^{\alpha\beta} = \sum_i f_i c_i^\alpha c_i^\beta$ is the density kernel, which, as follows from equation 2.36, is the representation of the density matrix $\rho(\mathbf{r},\mathbf{r}')$ in the support function basis [33].

At this stage, the Kohn-Sham orbitals have to be optimised by minimising the total energy with respect to the support functions and density kernel. Forced by the self-consistency of the method, this is equivalent to minimising the band structure energy E_{BS}, i.e.,

$$E_{BS} = \sum_{\alpha\beta} K^{\alpha\beta} H_{\alpha\beta}, \tag{2.38}$$

subject to the orthogonality condition of the Kohn-Sham orbitals

$$\psi_i^* \psi_j = \sum_{\alpha,\beta} c_i^{\alpha *} \phi_i^* \phi_j c_j^\beta = \delta_{i,j} \tag{2.39}$$

where

$$H_{\alpha\beta} = \langle \phi_\alpha | H_{KS} | \phi_\beta \rangle \tag{2.40}$$

is the Hamiltonian matrix in the support functions basis as in equation 2.26. Equation 2.39 is also equivalent to an idempotent density kernel, i.e., $K^2 = K$.

Up to this point, a new formalism has been introduced, but no extra approximation has been applied. Linear scaling of computational effort relies on the fact that the density kernel $K^{\alpha\beta}$ is *nearsighted* and hence, can be truncated for orbitals the centres of which are separated by more than some cut-off length. Hence, a natural and exact choice for these support functions would be the maximally localised Wannier functions[6], which have the same exponential decay [30].

Of course, these Wannier functions are not known beforehand. Therefore, the basis functions are constructed *in situ* and are expected to reach a quality similar to that of the exact

---

[6] The functions ϕ_α can be thought of as a combination of a subspace rotation $\mathbf{M}(\mathbf{k})$ of the Bloch orbitals at each $\mathbf{k}$ and a unitary transformation in $\mathbf{k}$-space, localising them to a super cell at position $\mathbf{R}$ [34]

$$\phi_\alpha(\mathbf{r}) = \frac{V}{(2\pi)^3} \int_{BZ} e^{-i\mathbf{k}\cdot\mathbf{R}} \left[\sum_i \psi_{i\mathbf{k}(\mathbf{r})} M_{i\alpha(\mathbf{k})} \right] d\mathbf{k}. \tag{2.41}$$

Wannier functions along a self-consistent cycle. The algorithm therefore consists of two key components: firstly, optimisation of the support functions and secondly, optimisation of the density kernel. The work-scheme 2.10 is based on a double loop structure, with the outer loop controlling the overall convergence, and two inner loops to optimise both the support functions and density kernel. The first of these inner loops is done non-self-consistently (i.e., with a fixed potential), whereas the second one is done self-consistently [33].

2.3.3 Particularities of metallic systems

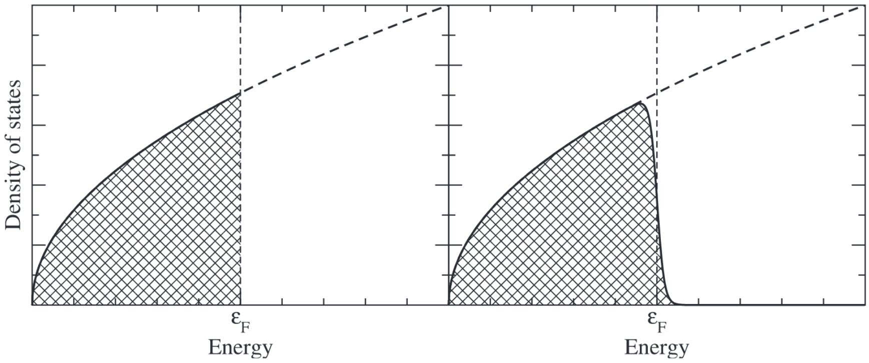

Fig. 2.3 Schematic illustration of the density of states (DOS) in a metal depending on their energy. The dark region represents the energy distribution of the electrons in each system. The left-hand panel shows the density of states without smearing; the right-hand panel shows it with smearing. Image from [39].

When using periodic boundary conditions, the electron density of the system becomes an integral over the 1st Brillouin zone in reciprocal space. In practice, this integral is evaluated by summation over a finite number of k-points (points in the reciprocal space). One major problem in the case of metals arises from the fact that the metallic energy levels are very close to one another. Thereby, the gap between the highest occupied and lowest unoccupied orbitals (HOMO and LUMO gap) is very narrow and the transition between occupied and unoccupied orbitals is sudden and difficult to localise. In this case, the function being integrated is discontinuous, what dramatically decreases the accuracy of whichever finite set of k-points in the Brillouin zone and complicates reaching convergence along the self-consistent cycle [39].

The most interesting technique to overcome this problem consists in increasing the temperature of the system slightly; as seen in equation 2.20 and figure 2.3, this smooths the functions at the Fermi level and facilitates convergence. However, this comes with a price: a new functional with electronic temperature different than $0K$ is calculated instead of the real one, what has the advantage that also assures the exponential decay of the density matrix with respect to distance. Indeed, usually temperatures of thousands of degrees need to be considered [40]. The error arising from this fact must be considered carefully.

On top of that, due to their conductivity and the delocalisation of electrons, the *nearsightedness* is less pronounced for metals than for insulators. The application of linear scaling DFT to metallic systems has been rather limited until now that a strategy to overcome those limitations has been set, and its validity and limitations are still to be determined.

2.4 Wavelets

Yet a last aspect needs to be tackled in order to numerically solve the Kohn-Sham equations; the choice of the basis used to represent the support functions ϕ_α of the Kohn-Sham orbitals. From a computational point of view, this is one of the most important characteristics of a DFT code [41].

Most of the DFT implementations work with plane waves or Gaussian basis sets. Due to their non-localised nature, plane waves are certainly suitable in the case of periodic and/or homogeneous systems but inefficient in expanding localised information. Gaussian basis, which stand out in this last feature, happen to be non-systematic[7], so over-completeness may be achieved before convergence. Wavelets are just another basis set, that is orthogonal, systematic, and at the same time localised and adaptive.

2.4.1 The Haar wavelet family, an iconic approach to wavelets

In order to introduce the reader to the concept of wavelet, the Haar wavelet family [42] is presented [43]. The Haar wavelet function, represented in figure 2.4, is the simplest wavelet family.

Any wavelet family comprises two fundamental functions, namely, the scaling function ϕ and the wavelet Ψ. To obtain a basis set at a certain resolution level k, we can use all the integer translations of the scaling function

$$\phi_i^k(x) = \phi(2^k x - i). \tag{2.42}$$

---

[7] Given a Partial Differential Equation, a *systematic basis set* enables the calculation of its solution with arbitrarily high precision as the number of basis functions is increased.

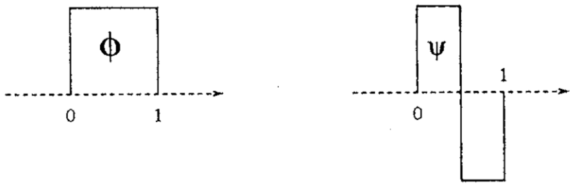

Fig. 2.4 The Haar scaling function ϕ and the wavelet ψ. Image from [43].

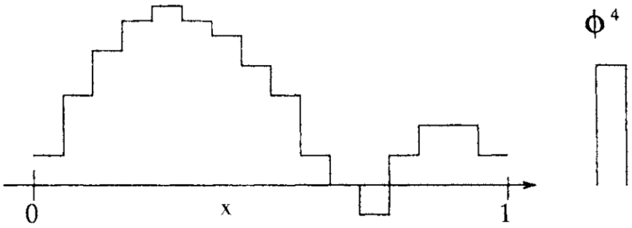

Fig. 2.5 Piecewise constant function f by means of the scaling-function of the Haar wavelet at resolution level 4 and the scaling function of the same resolution. Image from [43].

Notice that with this convention, higher resolution corresponds to larger values of k. Exactly the same scaling and shifting operations can also be applied to the wavelets

$$\psi_i^k(x) = \psi(2^k x - i). \tag{2.43}$$

In the case of the Haar family, any function that can exactly be represented at any level of resolution is necessarily piecewise constant. One such function is shown in figure 2.5. This function can be written in a scaling function representation as

$$f = \sum_{i=0}^{15} s_i^4 \phi_i^4(x), \tag{2.44}$$

where $s_i^4 = f(i/16)$. A wavelet representation is possible because a scaling function at

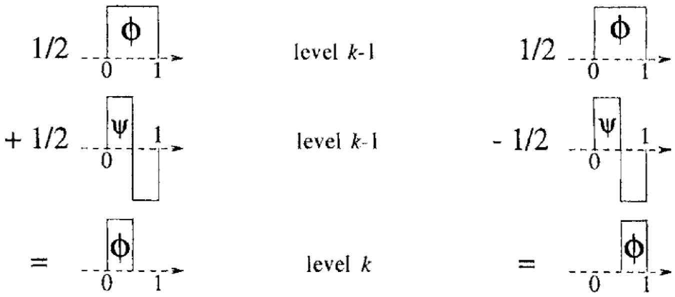

Fig. 2.6 A skinny (level k) scaling function is a linear combination of a fat (level $k-1$) scaling function and a fat wavelet. Image from [43].

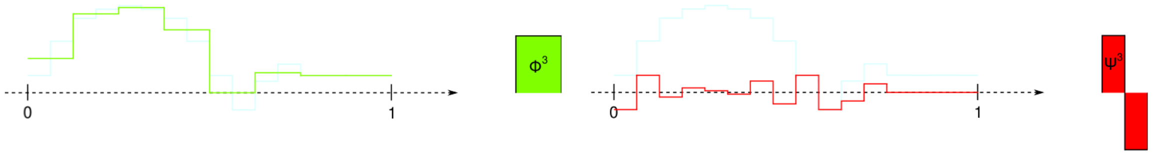

Fig. 2.7 Scaling function ϕ (left) and wavelet ψ (right) functions contribution, as expressed in equation 2.45. Notice how the scaling function is "smooth", while the wavelet experiences sudden changes. Image from [44].

resolution level k is always a linear combination of a scaling function and a wavelet at the next coarser level $k-1$ [43], as shown in figure 2.6. Using this property, f is rewritten as

$$f = \sum_{i=0}^{7} s_i^3 \phi_i^3(x) + \sum_{i=0}^{7} d_i^3 \psi_i^3(x). \tag{2.45}$$

It is easy to verify that the transformation rule for the coefficients is given by

$$s_i^{k-1} = \frac{1}{2} s_{2i}^k + \frac{1}{2} s_{2i+1}^k \quad ; \quad d_i^{k-1} = \frac{1}{2} s_{2i}^k - \frac{1}{2} s_{2i+1}^k. \tag{2.46}$$

This transformation can be repeatedly applied to any data set whose size is a power of 2. In each step the number of s coefficients will be cut into half, and the procedure has to be stopped when only one s coefficient is left. Such a series of transformation steps is called a *forward Haar wavelet transform*. The resulting wavelet representation of the function f is

$$f = s_0^0 \phi_0^0(x) + d_0^0 \psi_0^0(x) + \sum_{i=0}^{1} d_i^1 \phi_i^1(x) + \sum_{i=0}^{3} d_i^2 \psi_i^2(x) + \sum_{i=0}^{7} d_i^3 \psi_i^3(x). \tag{2.47}$$

Notice that the total number of expansion coefficients is kept equal to 16 among equations 2.44, 2.45 and 2.47, so the load of information is kept. Figure 2.7, which depicts the wavelet and scaling contributions, shows how the scaling function represents a smoothed version of f, while the wavelets represent the rapidly varying corrections to the smoothed function [8]. Actually, the contribution of the wavelet is rather localised; some of the wavelet coefficient may be zero, which may allow compression of data.

If wavelets are to be implemented to solve the Kohn-Sham equations 2.25-2.26, the chosen set needs to be three dimensional. On top of that, the application of the kinetic energy operator $\frac{1}{2}\nabla_i^2$ from 2.5 requires them to be differentiable, what they fortunately can be [45].

---

[8] In this particular case the word smooth may lead to confusion, due to the non-continuous nature of the example function. In the continuous case, this assumption is more consistent.

2.4.2 Three dimensional wavelets

The easiest way to construct a three-dimensional basis set consists in forming products of one dimensional scaling functions and wavelets, as shown in table 2.1. This gives rise to one three-dimensional scaling function $\phi_{i,j,k}$, which is a product of three one-dimensional scaling functions, and seven three-dimensional wavelets $\psi^n_{i,j,k}$, which are products containing at least a one-dimensional wavelet.

Table 2.1 Three-dimensional scaling function $\phi_{i,j,k}$ and seven three-dimensional wavelets $\psi^n_{i,j,k}$.

$\phi_{i,j,k} = \phi(x-i)\phi(y-j)\phi(z-k)$	$\psi^4_{i,j,k} = \psi(x-i)\psi(y-j)\phi(z-k)$
$\psi^1_{i,j,k} = \psi(x-i)\phi(y-j)\phi(z-k)$	$\psi^5_{i,j,k} = \psi(x-i)\phi(y-j)\psi(z-k)$
$\psi^2_{i,j,k} = \phi(x-i)\psi(y-j)\phi(z-k)$	$\psi^6_{i,j,k} = \phi(x-i)\psi(y-j)\psi(z-k)$
$\psi^3_{i,j,k} = \phi(x-i)\phi(y-j)\psi(z-k)$	$\psi^7_{i,j,k} = \psi(x-i)\psi(y-j)\psi(z-k)$

The three-dimensional scaling functions and wavelets fulfil as well orthogonality and refinement relations which are generalisations of the ones for the one-dimensional case.

2.5 BigDFT; the code

BigDFT is a free quantum chemistry and solid state physics software that calculates the total energy, charge density, and electronic structure, as well as their derived quantities, of systems such as molecules or periodic/crystalline solids by means of DFT. In the own words of its developers:

"BigDFT is a DFT massively parallel electronic structure code that uses a wavelet basis set. GTH or HGH pseudopotentials are used to remove the core electrons. Thanks to our Poisson solver based on a Green function formalism, periodic systems, surfaces and isolated systems can be simulated with the proper boundary conditions." [4]

2.5.1 Implementation of wavelets and resolution levels

BigDFT uses the least asymmetric Daubechies of order 16, which, as all the Daubechies wavelets, is asymmetric, orthogonal, differentiable and has compact support[9]. Figure 2.8, shows the scaling and wavelet functions of this family; notice the functions are continuous.

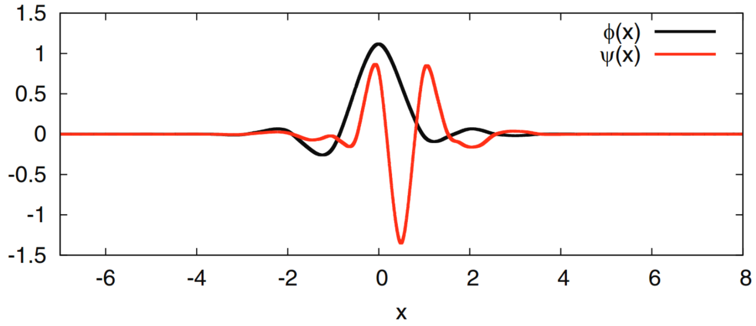

Fig. 2.8 Least asymmetric Daubechies wavelet family of order $2m = 16$; both the scaling function $\psi(x)$ and wavelet $\phi(x)$ differ from zero only within the interval $[1-m, m]$. Image from [33].

As already seen in section 2.4.1, one of the advantages of wavelets is the fact that they allow different levels of resolution (see figure 2.9). Since the grid spacing is constant along the simulation box, the different resolution levels are obtained by associating a number of scaling and wavelet functions to each grid point depending on the region they belong to. This feature enables a further optimisation of computational resources. BigDFT allows three levels of resolution:

i. High resolution for the region closer to the nuclei (i.e., fine region), for which each grid point is assigned a scaling function and seven wavelets.

ii. Medium resolution for the grid points further apart from the nuclei (i.e., coarse region), since the functions in this region tend not to change abruptly. Its resolution is half that of the fine region because only one scaling function and no wavelet are assigned per grid point.

iii. Points even further away from the nuclei, which do not contribute in any way to any of the previous regions are not considered.

Given a fine radius r, the fine region is the region of space defined by the union of all spheres with radii r centred at each of the nuclei. Given a coarse radius R, so that $r < R$, the coarse region is defined analogously, as the space defined by the union of all spheres with radii R

---

[9] A function has *compact support* if it is zero outside of a compact set.

centred at each of the nuclei minus the fine region. The value of r and R is assigned by the product of an atom-dependent constant and a user-specified factor.

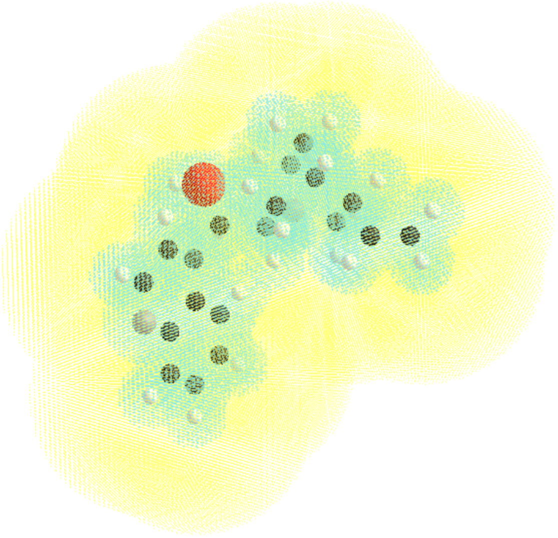

Fig. 2.9 Visualisation of the fine (green) and coarse (yellow) regions for *cinchonidine* ($C_{19}H_{22}N_2O$). Image from [33].

2.5.2 Implementation of the linear scaling approach

In section 2.3.2, the theoretical background of the linear scaling approach has been presented. In the following lines, the several steps used in BigDFT to exploit the decay properties of the density matrix elements are discussed.

Wavelets, support functions and orbitals

BigDFT is based on support functions $\phi_\alpha(\mathbf{r})$, which can be written in terms of wavelets ψ and scaling functions φ. In their turn, support functions express the orbitals. The benefit of this approach is that the dimension of the density matrix 2.37 is considerably reduced, while its quality is still preserved.

$$\phi_\alpha(\mathbf{r}) = \sum_{m=i,j,k} \left(s_m^\alpha \varphi_m(\mathbf{r}) + \sum_{\nu=1}^{7} d_{m,\nu}^\alpha \psi_m^\nu(\mathbf{r}) \right), \tag{2.48}$$

where α is the index of the support function. The set of support functions used in a particular simulation is optimised *in-situ* during the calculation. The cut-off length that delimits the *nearsighted* region and from which particles do not interact with each other any more, introduced along section 2.3.2, is defined as

$$s_m^\alpha = 0, d_{m,\nu}^\alpha = 0 \qquad \text{if } |\mathbf{r}_{i,j,k} - \mathbf{r}_\alpha| > R_{\text{cut-off}}. \tag{2.49}$$

Hybrid optimisation mode

The hybrid optimisation mode is responsible of optimising the support functions $\phi_\alpha(\mathbf{r})$. The quantity that needs to be optimised is

$$\Omega^{hy} = \sum_\alpha K_{\alpha\alpha}\phi_\alpha^* H_\alpha \phi_\alpha + \sum_{\beta\neq\alpha} K_{\alpha\beta}\phi_\alpha^* H \phi_\beta. \tag{2.50}$$

H_α is the Hamiltonian H plus the extra factor that creates the confining potential. Notice that, as the confinement of the potential H_α is decreased, $H_\alpha \rightarrow H$, thus leading to the expression of the total energy.

Density kernel

Once the support functions are obtained, the density matrix can also be expressed by means of this new basis as in equation 2.37, and so can the band structure energy E_{BS} be (see equation 2.38). Using equation 2.37 and the fact that the density matrix ρ is sparse, a condition analogous to 2.49 can be written in terms of the density kernel

$$K^{\alpha\beta} = 0 \quad \text{if} \quad |\mathbf{r}_\alpha - \mathbf{r}_\beta| > R_{\text{cut-off}}, \tag{2.51}$$

where $\mathbf{r}_\alpha$, $\mathbf{r}_\beta$ are the central position of the support function $\phi_\alpha(\mathbf{r})$ and $\phi_\beta(\mathbf{r}')$ respectively.

FOE and direct diagonalisation

The choice of the method through which the density kernel is optimised controls a large factor of the total computational time of the simulation. Using one or another depends on the complexity and size of the system under study. The BigDFT's linear version allows the following methods:

i. **Fermi Operator Expansion (FOE):** The FOE method directly calculates the density kernel $K^{\alpha\beta}$ in the basis of the support functions. The particular expansion of the operator in BigDFT uses the Chebyshev polynomial expansion[10]. The most important feature of this method in terms of its applicability is that it scales linearly with the system size because it exploits the sparsity of the matrices. Nonetheless, its pre-factor is big and thus for small system sizes other methods might be preferable.

ii. **Direct diagonalisation:** Direct diagonalisation is the most straightforward method, since it optimises the density kernel by performing a direct diagonalisation of the Hamiltonian matrix in the basis of the support functions. It is very useful for small systems because of its small prefactor, but it ends up being prohibitively expensive for big ones due to its cubic scaling with the system's size, since it does not exploit the sparsity of the matrices.

In figure 2.10, the flowchart of the linear scaling BigDFT method is depicted. Notice there are two inner loops, one for the support functions, which is optimised by the hybrid mode, and one for the density kernel, which is either optimised by FOE or by direct diagonalisation. The outer loop controls the convergence to the final value.

---

[10] Chebyshev polynomials are a sequence of orthogonal polynomials which are related to de Moivre's formula $(\cos x + i \sin x)^n = \cos(nx) + i \sin(nx)$ and which can be defined recursively.

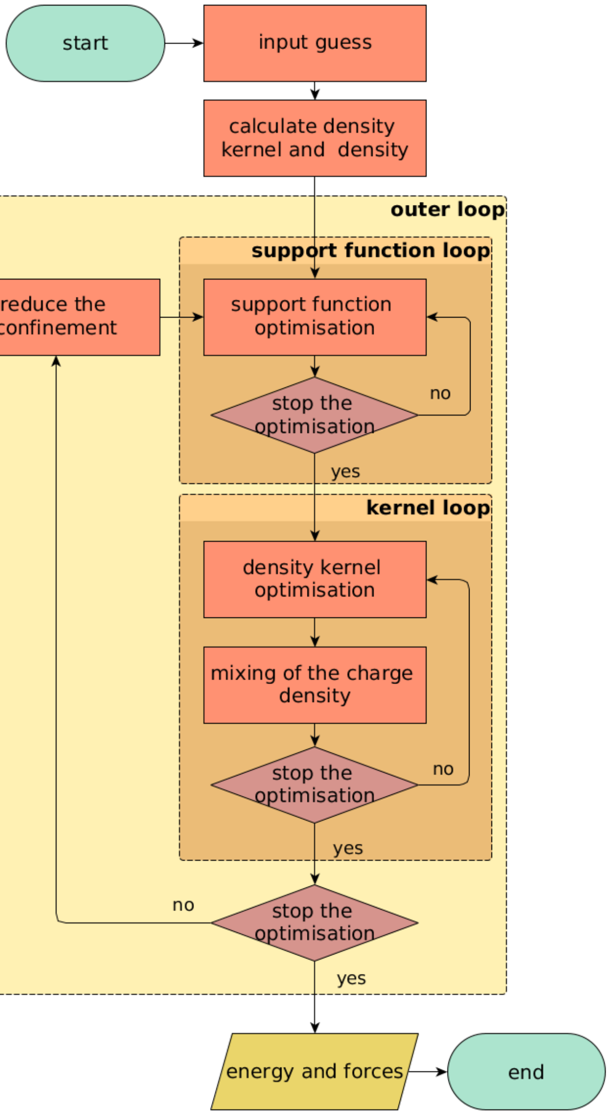
start
input guess
calculate density kernel and density
outer loop
support function loop
reduce the confinement
support function optimisation
stop the optimisation
no
yes
kernel loop
density kernel optimisation
mixing of the charge density
stop the optimisation
no
yes
no
stop the optimisation
yes
energy and forces
end

Fig. 2.10 Flowchart of the minimal basis approach: for the basis optimisation loop the hybrid scheme is used, and for the kernel optimisation loop either direct minimisation or the Fermi operator expansion method can be used in place of diagonalisation. Modified image from [33].

Chapter 3

Study of point defects by means of BigDFT

A fundamental description of defects on the atomistic scale requires the use of truly *ab initio* models, such as DFT, which set the basis upon which models of higher scales are built. As discussed along section 2.3, though, the study of point defects in W-crystals is a challenging problem in terms of convergence of the simulation. Calculations regarding single defects provide key point results such as lowest energy configuration of defects with high precision. The calculations performed from scratch, however, are very time consuming and do not succeed at describing the energy formation of those defects, and a new approach using pre-calculated fragments will be considered.

The calculations were conducted on High Performance Computers, mainly in MareNostrum but also in Marconi, with a peak of 4608 cores running in parallel for the same simulation. It is clear that being able to keep a good scaling for this amount of resources requires of a deep implementation of MPI and OpenMP in BigDFT.

3.1 Brief introduction to point defects

Nuclear reactions produced within the plasma in a fusion device generate highly energetic neutrons and charged particles. Whenever these particles collide into the wall of a magnetic confinement device, important changes in its physical and mechanical properties can arise; if the microstructure of the material forming the vessel is changed, its physical behaviour may be affected. Under irradiation, a material may suffer of mainly two types of radiation damage:

i. Structural distortions in the atomic structure (*i.e.*, radiation defects or simply defects), principally vacancies and self-intersticial atom defects (SIAs).

ii. Changes in the chemical composition of the material (*i.e.*, transmutation reactions).

Along this work the scope is limited to the first group of defects. Vacancies and SIAs form as a result of a process in which an atom is displaced from a lattice site and settles some distance away from its initial position, and hence such vacancies and SIAs always form in pairs, termed Frenkel pairs. In such a situation, the initially occupied lattice position becomes a vacancy (see figure 3.1a) and the moved atom forms a SIA in its new position (see figure 3.1b).

The formation energy of a vacancy (VFE) is calculated by means of the following equation

$$E_f(\text{vacancy}) = E_{N-1}(\text{relaxed}) - \left(\frac{N-1}{N}\right) E_N(\text{perfect}), \tag{3.1}$$

where $E_{N-1}(\text{relaxed})$ is the total energy of the simulation cell having removed one atom and $E_n(\text{perfect})$ is the energy of an N-atom cell without any defect. Analogously, the formation energy of a SIA defect is defined as

$$E_f(\text{SIA}) = E_{N+1}(\text{relaxed}) - \left(\frac{N+1}{N}\right) E_N(\text{perfect}) \tag{3.2}$$

where $E_{N+1}(\text{relaxed})$ is the total energy of a simulation cell containing an extra atom [3].

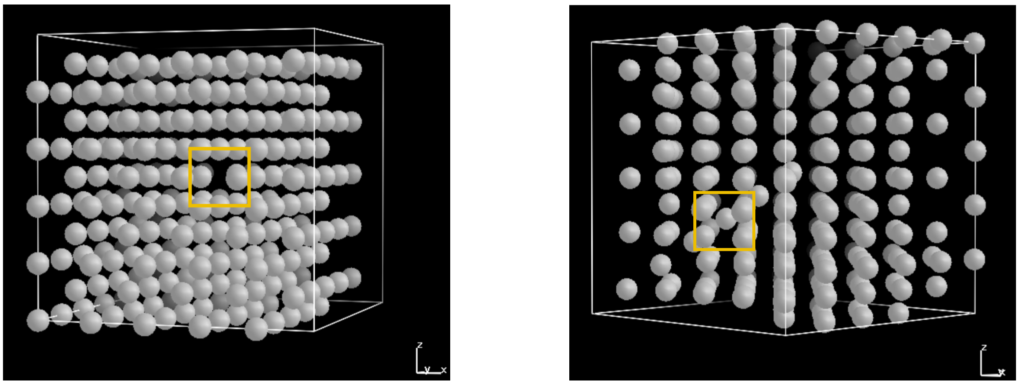

(a) Visualisation of a vacancy. **(b)** Visualisation of a crowdion SIA defect.

Fig. 3.1 Scheme of two different point defects in a 250-atom W-crystal, which together constitute a Frenkel pair.

This type of radiation damage needs a multiscale analysis in order to be properly understood. The starting point of defects happens on an atomistic scale, such as a single vacancy or a single self-interstitial atom (SIA). This is the object of study of this work. However, apart from a few remarkable exceptions described in [3], in all metals with closed-packed crystal structures, these point defects tend to form clusters that could end up requiring other types of models. On the mesoscopic scale the cascades may lead to a particular type of microstructural evolution [3].

3.2 *Ab initio* W-crystal simulations by means of BigDFT

A fundamental description of defects on the atomistic scale requires a computational approach. Particularly, it requires the use of truly *ab initio* models (*i.e.*, computational chemistry methods based on quantum chemistry) such as DFT. Those *ab initio* approaches form the basis upon which models of higher scales are built. Calculations regarding single defects provide key point results such as lowest energy configuration of vacancies with high precision, which are the subject of study of this thesis.

In order to obtain the value of the VFE, two DFT simulations need to be performed: one for the perfect structure and one for the defect structure. To do so, a set of *ab initio* calculations were run by means of BigDFT, as described along Chapter 2 and summarised in figure 2.10. It is important to point out that not only the perfect configurations, but also the defect ones, are assumed to be relaxed. Removing an atom from a lattice changes the forces between its atoms, what destabilises the system. Relaxing the system means hence moving the affected atoms so that the forces cancel out and the system reaches a new equilibrium. This procedure may be very time consuming when performed with DFT codes, so LAMMPS [46], a non-*ab initio* force field code, has been used instead. Even though some error may arise as a result of using a non-*ab initio* tool, this is assumed to be very small once the potential is accurately parametrised using *ab initio* simulations. Oppositely, the consequences of ignoring the relaxation of the structure would have been of great significance, with differences on the VFEs that could have surpassed $1eV$ from its real value [47].

In particular, and as introduced in Chapter 1, the research is focused on periodic structures of W-cells containing between 128 (4^3 minimal cells) and 1024 atoms (8^3 minimal cells) in the perfect case and one atom less in the defect one. From now on, the systems will be named by the number of atoms of their cells in the perfect case, so that, for example, the VFE of a 250-atom system will refer to the energy required to remove an atom from a 250-atom system. For consistency, the parameters presented in table 3.1 have been kept constant along the different approaches and simulations.

Table 3.1 Set of basic parameters used to run the different calculations in the full system approach.

linear method	direct diagonalisation
temperature [a.u.][1]	10^{-3}
electronic configuration	$6s^2\ 5d^4$
support functions per atom	9

3.3 Full system approach

The first approach to the VFE was a set of simulations that followed the flowchart seen in figure 2.10. Figure 3.2 plots the total energy per atom of both the perfect and defect cases depending on the system size, while table 3.2 shows the energy required to remove an atom from the grid. The energy values plotted in figure 3.2 are normalised, meaning that the total energy has been divided per the number of atoms to enable comparison among systems of different sizes, whereas the VFE values have been directly obtained from the total energies and by means of equation 3.1.

In figure 3.2, it is observed how the energy values of both the perfect and defect systems stabilise as the system's size grows, and some convergence can be foreseen. One should notice that convergence needs to be checked by studing the energy differences instead of the percentage errors, because energy is no absolute grade but a value susceptible of being added any scalar constant. The energy difference between the first two sizes is about $0.2eV$, while the one for the last pair decreases to $0.02eV$, a 10% of the first one; clearly, reaching convergence requires a large number of atoms.

When comparing the energy values of the perfect crystal with the ones of the crystal with vacancy one observes that the relative effect of the vacancy decreases with the rise of the number of atoms. It is hence reasonable to think that the vacancy inside the defect structure does not affect the global lattice and only adds a small perturbation, which becomes less apparent for bigger lattices. This pattern is more clearly observed in the $E_f(\text{vacancy})$ values given in table 3.2, where no relation between the VFE and the size of the system can be

---

[1] $1\text{ a.u.} = 3.1577464(55) \times 10^{-5} K$

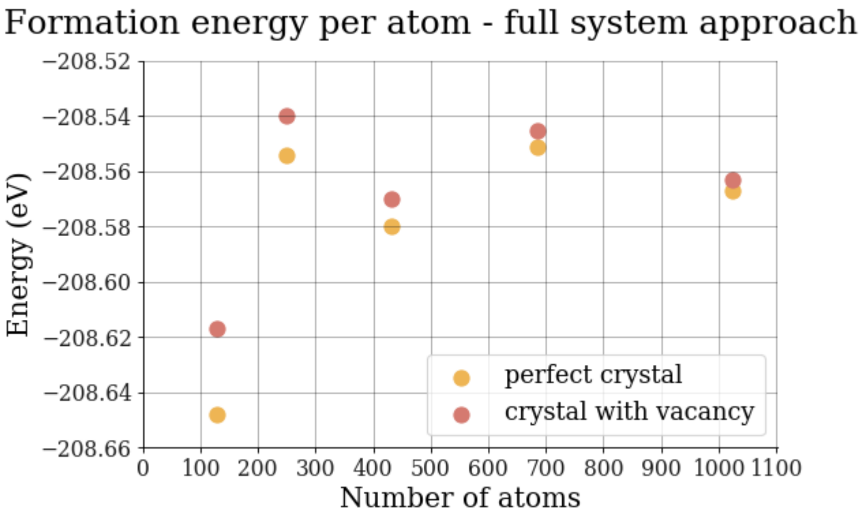

Fig. 3.2 Energy per atom in the full system approach calculations both in the perfect and defect cases.

Table 3.2 VFE of the full system approach depending on the number of atoms in the cell.

number of atoms	128	250	432	686	1024
$E_f(\text{vacancy})\ [eV]$	3.908	3.284	4.196	3.458	3.896

established. Instead of that, the VFE seems to "jump around" without converging to any value, but still keeping close to the reference theoretical value of $3.56eV$ [49], which was evaluated using the PLATO code [48].

The fact that the VFE cannot be clearly determined may be due to a bad signal-to-noise ratio; we look for energy differences that are very small compared to the total energy of the system (around 0.01%). However, even though larger systems would be required to get the energy of the lattice to converge, the systems under study in this thesis may suffice to describe the VFE. If the signal-to-noise ratio could be ameliorated, one would expect the VFE to stabilise and become constant. An hypothesis is that the problem is related to a dependency of the "convergence rate" of the support functions on the cell size. In the following chapter, a new approach to the problem is presented in which the support functions are kept the same regardless of the cell size, be it 250 atoms or 1024.

3.4 Fragment approach

The central idea of the fragment approach is to take a group of atoms and fully optimise its support functions [50]. These support functions are then used as a fixed basis for different systems containing those fragments. The interpolation of the template basis rototranslated to its new positions results in only a negligible loss of accuracy [50] and, since the support functions can be directly reused, it guarantees them to have the same "convergence rate" across various systems. This approach also reduces the computational cost of the calculations by one order of magnitude, compared to optimising the support functions from scratch in the full system approach.

As seen in figure 3.3, this approach modifies slightly the optimisation process shown in figure 2.10. In the image, and from now on, the first calculation, in which the support functions are generated, is referred to as *template*, while the second calculation, the one that uses the functions produced by the *template* calculation, is named *fragment*. Notice that the *template* calculation is run just once per fragment configuration. Since the functions are not optimised for each *fragment* calculation of different size, the fragment approach uses a slightly worse set of support functions, but at least consistent between the different system sizes. If the problem in the full system approach is to do with a difference in the "convergence rate" of the support functions of the different systems, it might be solved through this approach.

But how do we determine the fragments? If the system under study was made up of molecules or was a protein, one could think of clearly defined fragments corresponding to those isolated molecules or amino acids, and one could assign, for example, a charge to each piece [51]. The metallic crystal case, however, is a system in which the charge is non-localised, and the fragments are not so well defined nor can they be considered independently from one another. Consequently, the problem has been approached from different sights that will be described along the following lines. In any case, and oppositely to the representation of well defined substructures where the *templates* consider isolated fragments, the fragments were already built within the periodic crystal. Whenever the fragments are well defined, the *template* of those fragments is run considering the fragments as free clusters in an isolated environment. In our case, though, we consider them already to be within the periodic metallic environment.

In particular, the fragments were defined in periodic 250-W-atoms structures, or rather periodic 250-W-atoms structures with vacancy (i.e., 249-W-atoms periodic structures). Only the *template* of the 1 fragment case was built in a perfect 250-atoms cell periodic structure (i.e., without vacancy). From the 2 fragments on, they all were built in a periodic 250-atom cell structure with vacancy. Then, the fragments were understood to be related to the distance

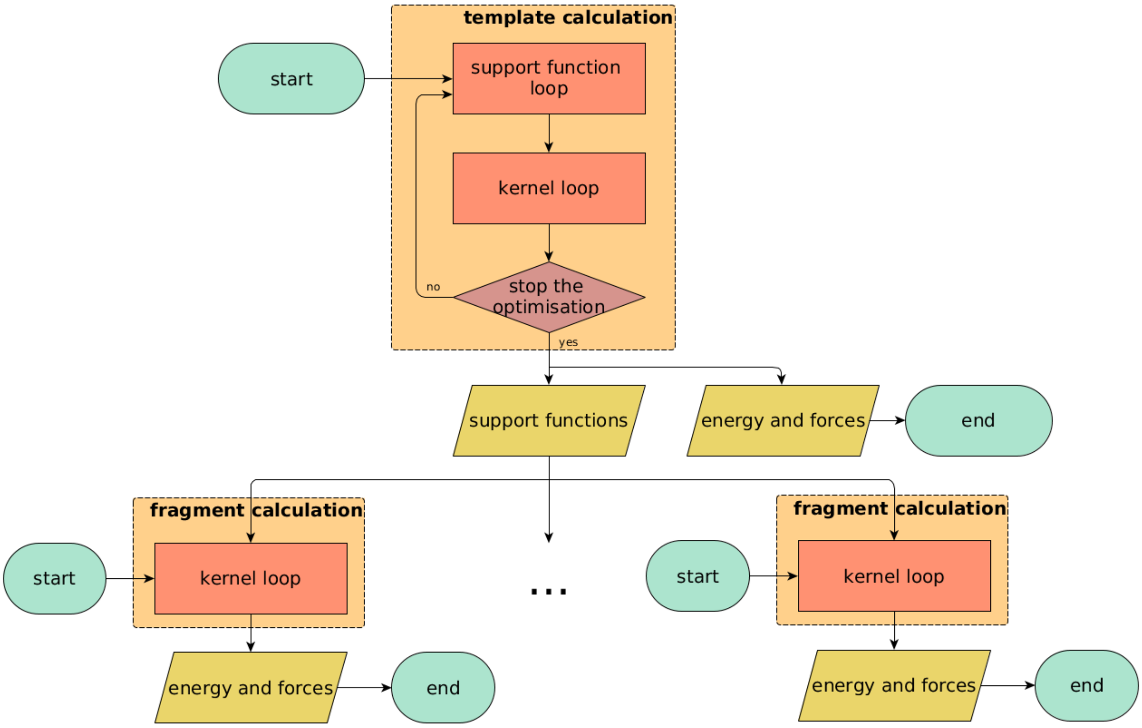
template calculation
start
support function loop
kernel loop
no
stop the optimisation
yes
support functions
energy and forces
end
fragment calculation
start
kernel loop
energy and forces
end
...
fragment calculation
start
kernel loop
energy and forces
end

Fig. 3.3 Flowchart of the fragment approach with one first template calculation and different fragment calculations. The template calculation is run for the 250-atom case and the generated support functions are used as templates for all the systems with the same fragmentation.

from the vacancy and defined as shells around the defect in an onion-alike way. Figure 3.4 shows the simplest fragmentations considered - excluding the 1 fragment case, which would be very similar to figure 1.2b, just containing 250-atoms instead of 128. Further details on the definitions of fragments are presented in sections 3.4.1 and 3.4.2.

The reason why the system containing 250 atoms, and not the one containing 128, was taken as a reference along the fragment approach is described in [1]. In its charge analysis, one observes how a vacancy modifies appreciably the internal monopole distribution in such a small system, what could affect the interaction with neighbouring periodic cells. On top of that, [1] also shows that such a small system does not get the atomic monopoles to be neutral in the perfect structure. This prevents the calculation of being in the converged range, what agrees with the results presented in section 3.3.

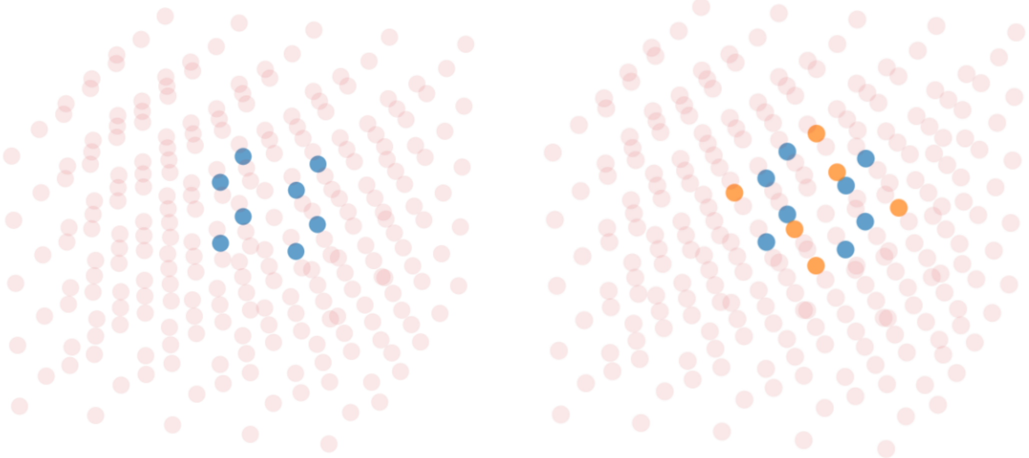

(a) 2 fragments **(b)** 3 fragments

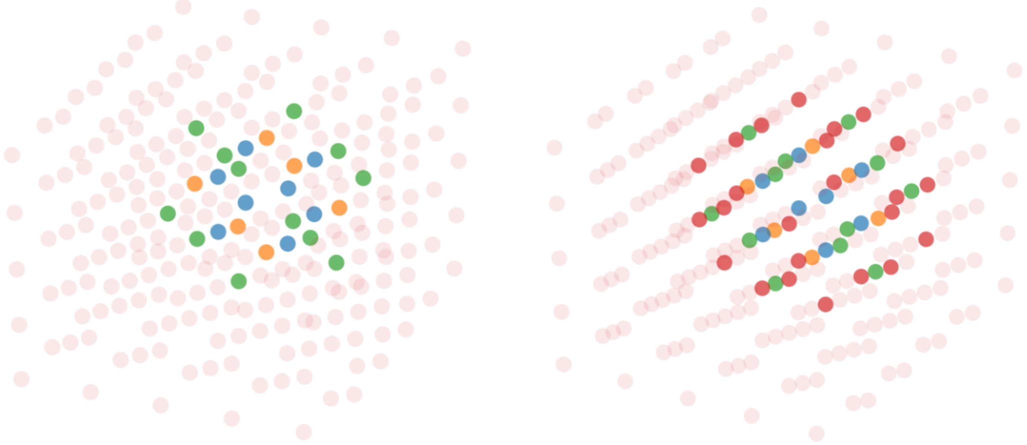

(c) 4 fragments **(d)** 5 fragments

Fig. 3.4 Visualisation of the fragments in a 250-atom cell with vacancy depending on the number of fragments considered. Atoms are represented by coloured spheres centred at their nuclei's position. The ones painted in blue are placed at the 1st fragment, the ones in orange at the 2nd, the ones in green at the 3rd fragment and the ones in light red at the 4th, while translucent pink spheres represent all the atoms contained in the last fragment.

3.4.1 Atomic fragments

Since the criterion to identify a fragment within a metallic periodic system is not clearly defined, the first approach to fragments was done considering 1-atom fragments. This is, the atoms within a given set of fragments were considered equivalent to generate a set of support functions that would then be applied independently to each of those atoms. The VFE equation 3.1 requires the energy of both the perfect and defect systems, and both were here approached through atomic fragments. To start with, figure 3.5 plots the results of the perfect systems, which have been calculated by using the support functions generated within the perfect 250-atom system in the different perfect systems.

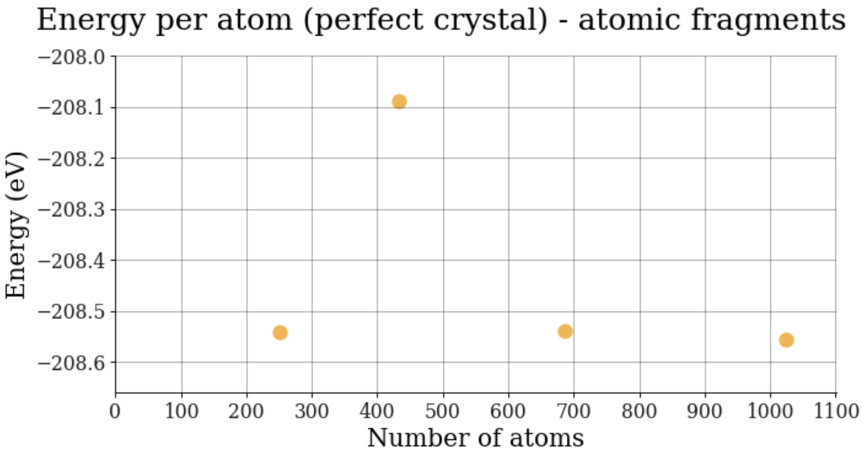

Fig. 3.5 Energy per atom for different crystal sizes in the perfect configuration calculated by means of the atomic fragment approach.

When comparing these results with the ones plotted in figure 3.2, the most interesting feature one observes is how the energy of the 432 system differs considerably, and differentiates from the rest of energies in the atomic fragment approach. We will come back to this issue in section 3.4.2, once we can determine the VFE using the fragment approach. In any case, determining the energy of perfect systems using support functions created in a perfect crystal seems sensible, and these results will be set as $E_N(\text{perfect})$ during the whole fragment approach.

Having determined the energy of the perfect crystals, we now focus on the determination of the energy in the defect crystal; the one with the vacancy. To start with, we focused on the 250-atom system case (i.e., due to the vacancy, this system actually contains 249 atoms), so that not only the *template* calculation but also the *fragment* computations were run considering the periodic 249-atom system (remember that only the 1-fragment *fragment* computation is based on the perfect 250-atom cell, while from the 2-fragment *fragment* computation on the support functions are produced in the 249-atom system). The resulting VFEs are plotted in figure 3.6.

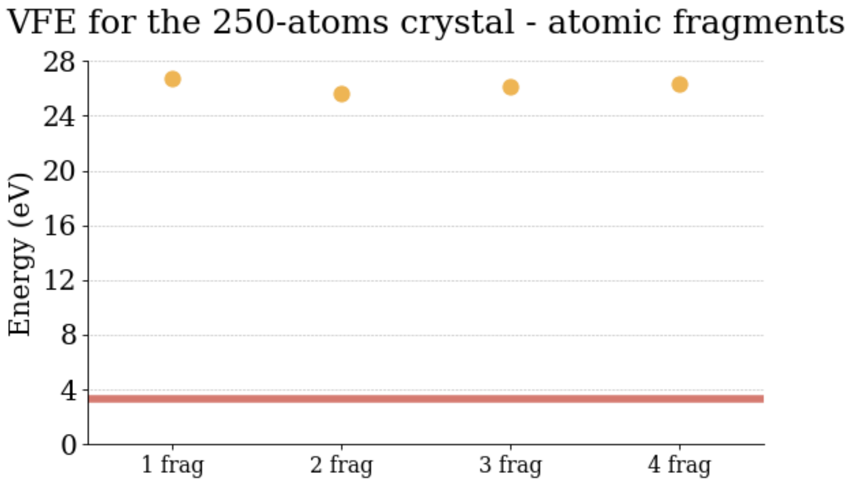

Fig. 3.6 VFEs for different atomic fragmentations dispositions for the 250-atoms crystal with vacancy. The result for the full system is plotted in red as reference.

In the graph, it is observed how the obtained VFEs have nothing to do with the expected ones, which should be similar to the full system result (plotted as a red line). This result is not surprising for the 1 fragment case (corresponding to the perfect system), in which the support functions were determined without considering any vacancy. However, it is remarkable that adding further fragment classes, for which the *template* was already run in the default 250-atoms defect system, does not improve this result. This may be due to the symmetry constraint implicit in the way fragments have been defined; the functions seem to be unable to determine the position of the vacancy, as if they could not understand an atom is missing in a given position. Therefore, this atomic fragment definition ends up suppressing the effect of the vacancy and cannot describe the system properly.

3.4.2 Onion-alike cluster fragments

A new approach to identifying the fragment in this metallic periodic system is to consider the atoms in the previously defined fragments as a whole. This is, understanding the whole set of atoms within a fragment as a cluster, and aiming to find a set of support functions that describes it all together. Now the fragments have different sizes; they may be eight, six, twelve-atoms big... depending on the fragment (see figure 3.4). Only the last fragment, the one in translucent pink in figure 3.4, is kept atomic and the support functions defining it will be the ones of the perfect crystal (the ones used to produce the 1 fragment calculation in figure 3.6). This is also the case of the 1 fragment case.

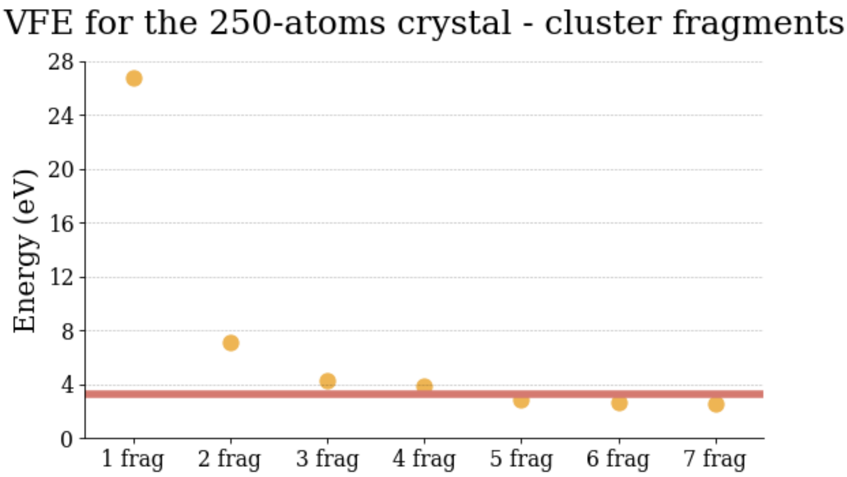

Fig. 3.7 VFEs for different cluster fragmentations dispositions for the 250-atom crystal with vacancy. The result for the full system is plotted in red as reference.

To start with, the 250-atom *fragment* case is considered. The resulting VFEs are plotted in figure 3.7. One observes how in this case the more fragments are included, the more similar the results of the full system and the fragment approach becomes. Having seen that this cluster fragment succeeds at reproducing the results obtained within the full system, we try to apply those support functions to bigger systems, i.e., we use the template support functions of the 250-atom system for the rest of systems. The results are plotted in figure 3.8. Notice that, since convergence in figure 3.7 seems to have been reached already for the 6 fragments case, we will restrict the study to up to 6 fragments from now on.

These results are clearly not reasonable; one observes an unexpected rise of the VFE in the 686-atom case. Due to time constrains, the energy of the 1024 system of neither the 5 fragment nor the 6 fragment calculations could be determined, but they are unlikely to become better. However, one can observe an improvement in the results along the implementation of the first fragments, which is better seen in figure 3.9, where the values bigger than $32eV$ have been suppressed. In this figure, we observe a progress similar to the one observed in the 250-atom case when considering the 1 fragment to the 3 fragment system range, also in the 432-atom case. This shows that the energy determined for the perfect 432-atom system through the atomic fragment approach is at least consistent with the energy in the defect case. This tendency, however, is abruptly broken when considering more fragments. The new values do not only get worse, but end up being comparable or even remarkably worse than the ones obtained in the 1 fragment case, where the support functions consider no vacancy.

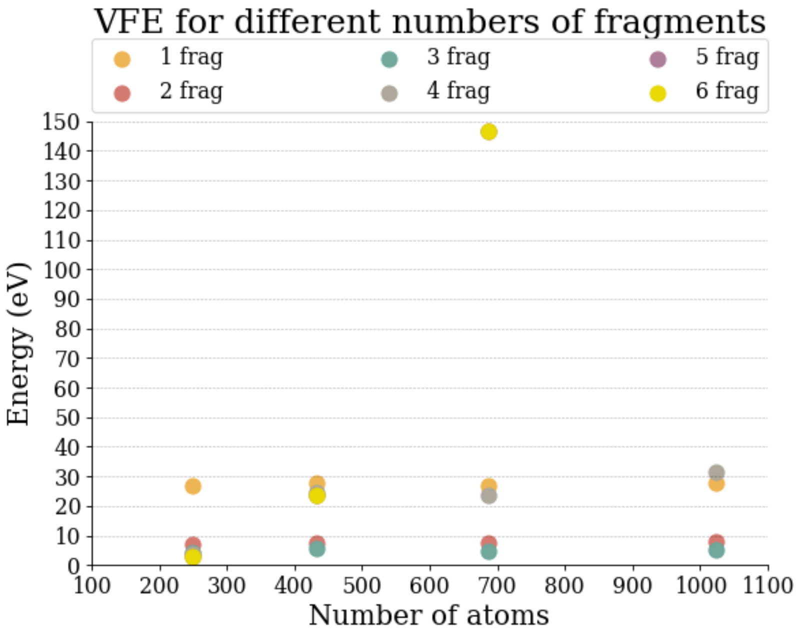

Fig. 3.8 VFEs for different cluster fragmentation dispositions and system sizes. The 5 fragment values may be difficult to see, because they are almost equal to the 6 fragment ones.

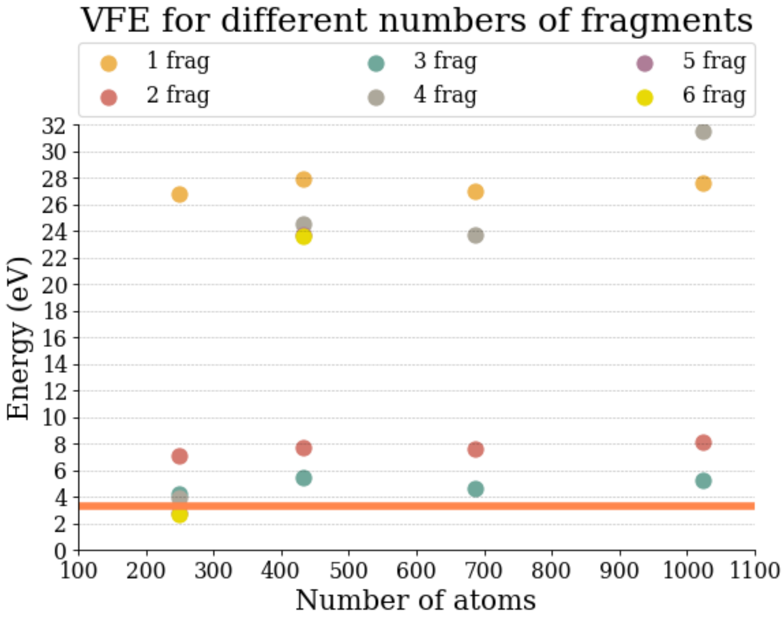

Fig. 3.9 VFEs up to $32 eV$ for different cluster fragmentation dispositions and system sizes. The result for the full system is plotted in orange as reference. The 5 fragment values may be difficult to see, because they are almost equal to the 6 fragment ones.

So far, we are unable to explain this change in the behaviour of the results from the four fragments on, but we suspect a bug in the code or en error in the set-up.

3.4.3 Two cluster fragments

To end up with, fragments have been approached from a third sight. This time only two cluster (i.e., not atomic) fragments have been defined, and the atoms within the cells have been split between atoms near the vacancy and atoms to be found far apart from the defect. This is, the opaque fragments plotted in figure 3.4 have been considered together in a new cluster fragment, called shell, as seen in figure 3.10. In this sense, for example, the 3rd shell system considers the opaque atoms in the 3 fragment case of image 3.4b to be contained in one only fragment, while the translucent ones are placed in an other fragment. Notice that the 1st shell case is still the same 1-fragment arrangement from the atomic case, while the 2nd shell system coincides with the 2-fragment one defined in the cluster fragment approach.

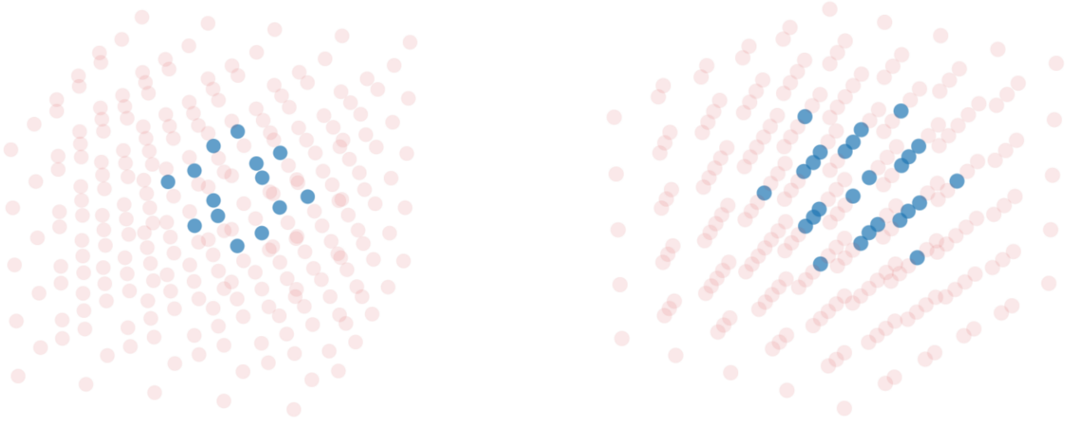

(a) 3rd shell **(b)** 4th shell

Fig. 3.10 Visualisation of the two cluster shells in a 250-atom system with vacancy. Atoms are represented by coloured spheres centred at their nuclei's position. The ones painted in blue are placed at the 1st fragment, while the ones in translucent pink constitute the 2nd one.

Again, we start by studying the 250-atoms cell case, the results of which are plotted in figure 3.11. We observe how these values are almost the same ones as the ones obtained along the cluster fragment approach, plotted in figure 3.7. Having seen that this cluster fragment also succeeds at reproducing the results obtained within the full system approach in section 3.3, we try to implement it in the bigger systems. The results are plotted in figure 3.12. As happened in the onion-alike cluster approach due to time constrains, the energy of the 4th to the 6th shell 1024 systems could not be determined. In this case, the plot has directly

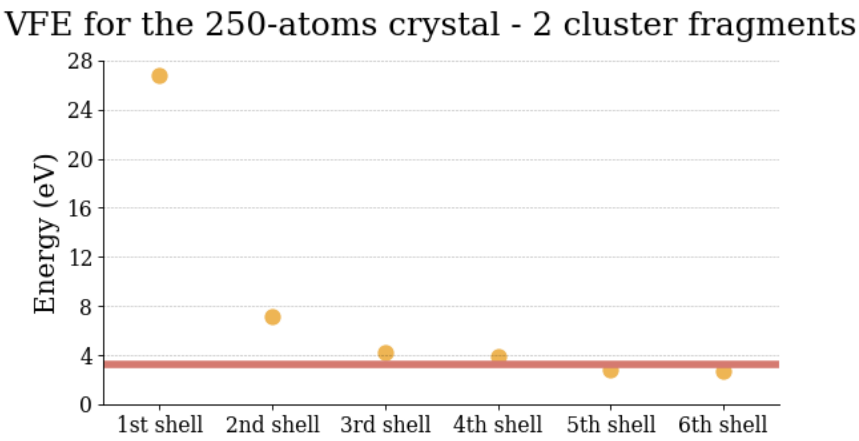

Fig. 3.11 VFEs for different two cluster-shell fragmentations dispositions for the 250-atom crystal with vacancy. The result for the full system is plotted in red as reference.

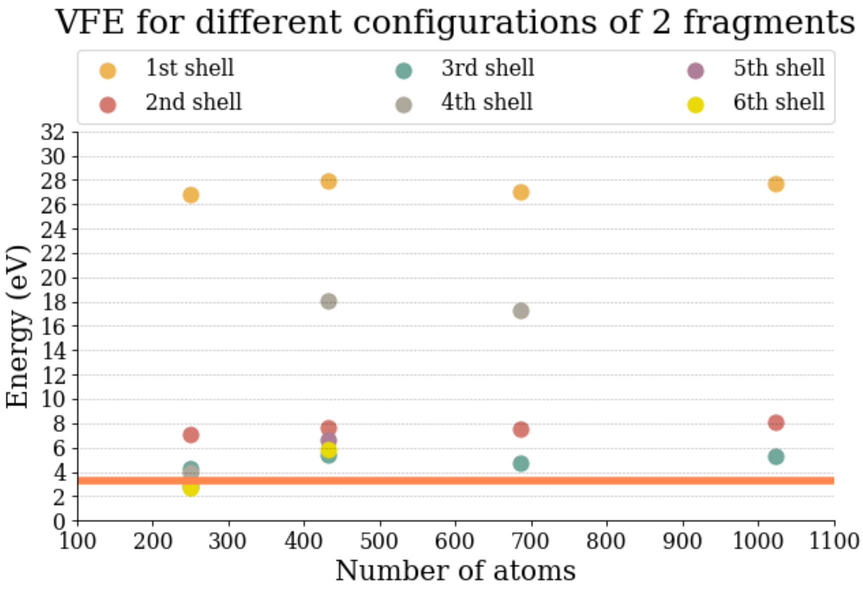

Fig. 3.12 VFEs up to $32eV$ for different 2 cluster fragmentations dispositions for the 250-atom crystal with vacancy. The result for the full system is plotted in red as reference.

been restricted to energies up to $32eV$, so the values obtained for the 5th and 6th shells in the 686-atom system (that gave a value of around $205eV$) are not to be found in the graph.

We observe how the results are somehow better than the ones obtained in the onion-alike cluster fragment approach and due to time constrains, the energy of the 4th to the 6th shell 1024 systems could not be determined. , but they are unlikely to become better. but still not satisfactory; one can still observe an unexpected behaviour from the 4^{th} shell system on for systems bigger than the 250-atom one. We may attribute this fact to a bug in the code or to an error in the set-up.

3.5 Brief study of the CPU time consumption

As explained at the beginning of chapter 3, a collateral benefit of the fragment approach is the reduction on time of the calculations. This can be seen in figures 3.13 and 3.14. The first one shows how, in the template calculation, the CPU time slightly increases with the number of fragments considered. However, this increase is almost insignificant. The fragment calculation does not increase with the number of fragments considered, and is about 40% quicker than the template one. Nevertheless, the fragment calculation depends on the previously generated support functions, for which a whole template calculation needs to be run. Hence, this reduction on time only reduces the final time consumption if more than three fragment calculations per template are considered.

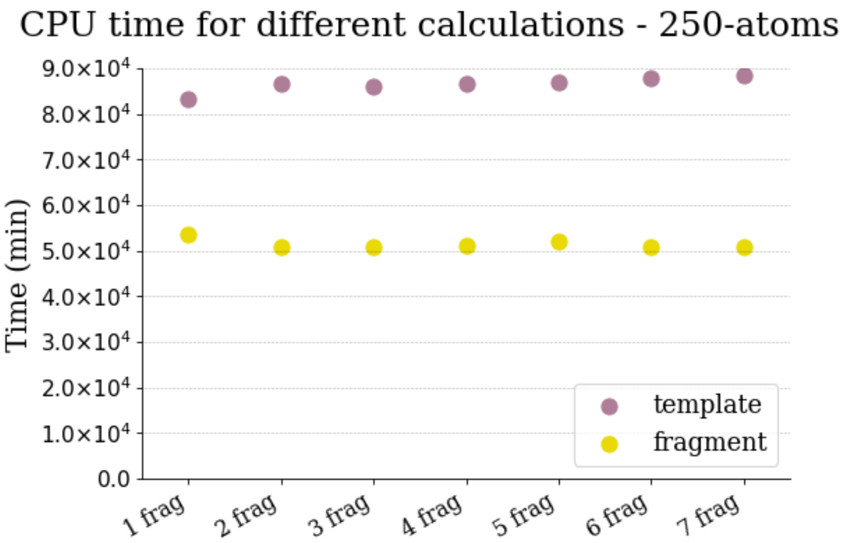

Fig. 3.13 CPU time since initialisation of the template and fragment calculations of different cluster fragmentation dispositions for the 250-atom crystal with vacancy.

The second figure correlates the CPU time consumption with the system size considered. Since in the previous image 3.13 the CPU time reminds almost constant, regardless of the number of fragments considered, figure 3.14 plots only the time corresponding to the 1 fragment template generation (which corresponds to the full system approach to those systems) and 1 fragment calculation (which corresponds to the implementation of the support functions generated within the perfect 2550-atom system in the bigger arrangements). We observe a quadratic dependency of time on the system's size and how, so we conclude that the systems are too small to suffer from the cubic limitation arising from the direct diagonalisation method that optimises the density kernel. Even though the proportion between full system and fragment approach time consumption decreases with the size, the impact of this difference becomes grater in absolute numbers.

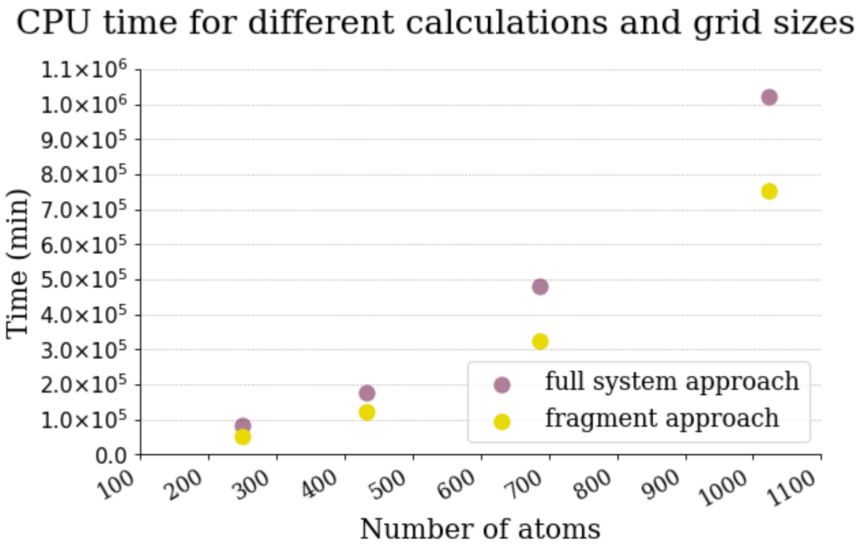

Fig. 3.14 CPU time since initialisation of the template and fragment calculations of different cluster fragmentation dispositions.

Chapter 4

Conclusions and future work

4.1 Conclusions

The aim of this work was to determine with precision the formation energy of a vacancy (VFE) in a W-crystal as a particular case of a radiation point defect. This should be a first step towards understanding the radiation damage such a crystal may suffer in a fusion reactor on the atomistic scale. At this scale, a fundamental description of defects requires a computational approach such as DFT, for what the BigDFT software was implemented. After seeing that a full system calculation is unable to describe the VFE with precision, three different implementations of the fragment approach have been studied in an attempt to finding out if the "convergence rate" of the different support functions produced for the different system sizes along the full system calculation interfered in the results.

The main contribution of this work is that a fragment approach implementation in BigDFT is able to describe a metallic crystal. Unlike in the case of molecules, the fragments along our implementation have been generated in a periodic environment, what has also been proved sensible. In particular, this has been proven successful for the 250-atom W-crystal system (and its corresponding defect structure containing 249 atoms), as shown in figures 3.7 and 3.11. Furthermore, it has been seen how the results of both the onion-alike cluster fragment and the two cluster fragment approaches tend to correlate to the full system calculation result the more or bigger fragments were considered.

Moreover, these fragment approaches have been proven successful along the implementation of the first fragments in bigger systems, when only the closest atoms to the vacancy were considered different from the rest. Nevertheless, it has been observed how this pattern cracks suddenly at a given point, i.e., when more fragments are defined in the onion-alike cluster case or if more atoms are included in the first shell in the two cluster fragment approach. We may attribute this fact to some bug in the code or error in the set-up. One would have also liked to have had a better understanding of the particular values of the 432-atom system (detected in figure 3.5), which nevertheless have not had any more implication in the VFEs values further than the one observed in the other systems.

A follow-up investigation would first need to explain this feature and correct any possible error committed along the described implementation or within the code if this is the case. One may then find out if the fragment approach is able to overcome the difference on the "convergence rate" of the support functions of systems of different sizes, and be able to unambiguously determine the energy formation of a vacancy in a W-crystal. Having done this, an implementation of the fragment approach for the study of the SIA defects may also be necessary in order to describe the whole Frenkel pair system.

References

[1] M. Eixarch Fernández. Ab-initio molecular dynamics for metallic systems. Master's thesis, Universitat Autònoma de Barcelona, 2017.

[2] EFDA European Fusion Development Agreement. *A roadmap to the realisation of fusion energy*. 2012.

[3] S. L. Dudarev *et al.* Density functional theory models for radiation damage. *Annu. Rev. Mater. Res.*, 43:35–61, 5 2013.

[4] BigDFT Contributors. Bigdft website. http://bigdft.org, 2013.

[5] P. Gerland *et al.* World population stabilization unlikely this century. *Science*, 346(6206):234–237, 2014.

[6] Iter organisation. Iter. https://www.iter.org/sci/whatisfusion, 2018.

[7] J. K. Shultis and R. E. Faw. *Fundamentals of nuclear science and engineering*, page 151. Marcel Dekker, Inc, 2002.

[8] A. Einstein. Ist die trägheit eines körpers von seinem energieinhalt abhängig? *Annalen der Physik*, 323(13):639–641.

[9] M. R. Gilbert *et al.* An integrated model for materials in a fusion power plant: transmutation, gas production, and helium embrittlement under neutron irradiation. *Nuclear Fusion*, 52(8):083019, 8 2012.

[10] H. Bolt *et al.* Materials for the plasma-facing components of fusion reactors. *Journal of Nuclear Materials*, 329-333:66 – 73, 2004. Proceedings of the 11th International Conference on Fusion Reactor Materials (ICFRM-11).

[11] H. Maier K. Krieger and R. Neu. Conclusions about the use of tungsten in the divertor of asdex upgrade. *Journal of Nuclear Materials*, 266-269:207 – 216, 1999.

[12] M. Tokitani *et al.* Plasma surface interaction on the surface of tungsten divertor tiles in lhd. *Journal of Nuclear Materials*, 415(1, Supplement):S87 – S91, 2011. Proceedings of the 19th International Conference on Plasma-Surface Interactions in Controlled Fusion.

[13] R.G. Parr and W. Yang. *Density-Functional Theory of Atoms and Molecules*. Oxford Science Publications, 1989.

[14] Wikipedia Contributors. Wikipedia, the free encyclopedia. https://en.wikipedia.org/wiki/Quantum_tunnelling.

[15] Ideen2020 - ein rundgang durch die welt von morgen. http://www.ideen2020.de/wp-content/uploads/slideshow-gallery/5_tokamak_stellarator_a_RGB.jpg.

[16] Y. Nemoto *et al.* Microstructural development of neutron irradiated w–re alloys. *Journal of Nuclear Materials*, 283-287:1144 – 1147, 2000. 9th Int. Conf. on Fusion Reactor Materials.

[17] R. A. Causey and T. J. Venhaus. The use of tungsten in fusion reactors: a review of the hydrogen retention and migration properties. *Physica Scripta*, 2001(T94):9, 2001.

[18] R. Neu *et al.* Tungsten as plasma-facing material in asdex upgrade. *Fusion Engineering and Design*, 65(3):367 – 374, 2003. 1st International Workshop on Innovative Concepts for Plasma - Interactive Components in Fusion Devices.

[19] M. Tokitani *et al.* Plasma surface interaction on the surface of tungsten divertor tiles in lhd. *J. Nuclear Materials*, 415(1, Supplement):S87 – S91, 2011. Proceedings of the 19th International Conference on Plasma-Surface Interactions in Controlled Fusion.

[20] H. Bolt *et al.* Materials for the plasma-facing components of fusion reactors. *Journal of Nuclear Materials*, 329-333:66 – 73, 2004. Proceedings of the 11th International Conference on Fusion Reactor Materials (ICFRM-11).

[21] E. Schrödinger. An undulatory theory of the mechanics of atoms and molecules. *Phys. Rev.*, 28:1049–1070, 1926.

[22] M. Born and R. Oppenheimer. Zur quantentheorie der molekeln. *Ann. Phys.*, 389:457, 1927.

[23] L. H. Thomas. The calculation of atomic fields. *Mathematical Proceedings of the Cambridge Philosophical Society*, 23(5):542–548, 1927.

[24] E. Fermi. Un metodo statistico per la determinazione di alcune priorieta dell'atome. *Rend. Accad. Naz. Lincei*, 6(602-607):32, 1927.

[25] P. Hohenberg and W. Kohn. Inhomogeneous electron gas. *Phys. Rev.*, 136:864–871, 1964.

[26] W. Kohn and L. J. Sham. Self-consistent equations including exchange and correlation effects. *Phys. Rev.*, 140:1133–1138, 1965.

[27] Shrinivas R. Kulkarni. Lectures 2-3. http://www.astro.caltech.edu/~srk/Ay126/Lectures/Lecture5/Lecture%202-3.pdf.

[28] T. Wegener. Physics in a nutshell. https://www.physics-in-a-nutshell.com/article/5.

[29] N. Marzari, I. Souza, and D. Vanderbilt. An introduction to maximally-localized wannier functions. http://www.psi-k.org/newsletters/News_57/Highlight_57.pdf, 08 2018.

[30] N. Marzari and D. Vanderbilt. Maximally localized generalized wannier functions for composite energy bands. *Phys. Rev. B*, 56:12847–12865, Nov 1997.

[31] K. Burke and L. O. Wagner. Dft in a nutshell. *Int. J. Quantum Chem.*, 113:96–101, 2013.

[32] E. J. Bylaska. Introduction to plane-wave basis sets and pseudopotential theory. http://www.nwchem-sw.org/images/Pw-lecture.pdf.

[33] S. Mohr *et al.* Daubechies wavelets for linear scaling density functional theory. *The Journal of Chemical Physics*, 140(20):204110, 5 2014.

[34] N. D. M. Hine *et al.* Linear-scaling density-functional theory with tens of thousands of atoms: Expanding the scope and scale of calculations with ONETEP. *Computer Physics Communications*, 180(7):1041 – 1053, 2009.

[35] W. Kohn. Density functional and density matrix method scaling linearly with the number of atoms. *Physical review letters*, 76:3168–3171, 05 1996.

[36] S. Goedecker. Decay properties of the finite-temperature density matrix in metals. *Phys. Rev. B*, 58:3501–3502, Aug 1998.

[37] S. Ismail-Beigi and T. A. Arias. Locality of the density matrix in metals, semiconductors, and insulators. *Phys. Rev. Lett.*, 82:2127–2130, Mar 1999.

[38] E. Hernández and M. J. Gillan. Self-consistent first-principles technique with linear scaling. *Phys. Rev. B*, 51:10157–10160, Apr 1995.

[39] B. G. Walker, C. Molteni, and N. Marzari. Ab initio molecular dynamics of metal surfaces. *Journal of Physics: Condensed Matter*, 16(26):S2575, 2004.

[40] N. Marzari. Theory and simulation of materials - electronic temperature. http://theossrv1.epfl.ch/Main/ElectronicTemperature.

[41] L. Genovese *et al.* Daubechies wavelets for high performance electronic structure calculations: The bigdft project. *C. R. Mecanique*, 339:149–164, 2 2011.

[42] A. Haar. Zur theorie der orthogonalen funktionensysteme. *Mathematische Annalen*, 69(3):331–371, 9 1910.

[43] S. Goedecker and O. Ivanov. Solution of multiscale partial differential equations using wavelets. *Computers in Physics*, 12:548–555, 11 1998.

[44] S. Mohr. *Fast and accurate electronic structure methods: large systems and applications to boron-carbon heterofullerenes*. PhD thesis, Universität Basel, 2013.

[45] K. McCormick and Raymond O. Wells Jr. Wavelet calculus and finite difference operators. *Math. Comput.*, 63(207):155–173, 7 1994.

[46] Lammps Contributors. Lammps molecular dynamics simulator. http://lammps.sandia.gov, 2013.

[47] P. Söderlind *et al.* First-principles formation energies of monovacancies in bcc transition metals. *Physical Review. B*, 61(4), 1 2000.

[48] A.P. Horsfield S.D. Kenny. Computer physics communications program library - plato: A localised orbital based density functional theory code. http://cpc.cs.qub.ac.uk/summaries/AEFC_v1_0.html, 2009.

[49] D. Nguyen-Manh, A. P. Horsfield, and S. L. Dudarev. Self-interstitial atom defects in bcc transition metals: Group-specific trends. *Phys. Rev. B*, 73:020101, Jan 2006.

[50] L. E. Ratcliff *et al.* Fragment approach to constrained density functional theory calculations using daubechies wavelets. *J. Chem. Phys.*, 142(23), 6 2015.

[51] S. Mohr *et al.* Complexity reduction in large quantum systems: Fragment identification and population analysis via a local optimized minimal basis. *J. Chem. Theory Comput.*, 142(9):4079–4088, 7 2017.